The aging-induced long non-coding RNA *MIRIAL* controls endothelial cell and mitochondrial function

Short title: The lncRNA *MIRIAL* in endothelial cells

Caroline Kohnle, MSc [1,2], Susanne Koziarek, Dipl. Nano-Sc. [1], Timothy Warwick, PhD [2,3], Kosta Theodorou, PhD [1], Ariane Fischer [1], Rio Putra Juni, PhD [5], Marion Muhly-Reinholz [1], Denise Busscher, MSc [1], Frederike Lam, PhD [2,3], Felix Vetter [1], Julian U. G. Wagner, PhD [1,2,4], Janina Sommer, MSc [1], Anna Theresa Gimbel, PhD [1,2], Laura Stanicek, PhD [1,5], Stefan Günther, PhD [2,4,6], Ilka Wittig, PhD [7], Lars Maegdefessel, PhD [8,9,10], Matthias S. Leisegang, PhD [2,3], Ralf P. Brandes, PhD [2,3,4], Stefanie Dimmeler, PhD [1,2,4], Reinier A. Boon, PhD [1,2,4,5,†]

Affiliations:

[1]Goethe University Frankfurt, Faculty of Medicine, Centre of Molecular Medicine, Institute of Cardiovascular Regeneration, Frankfurt am Main, Germany.
[2]German Centre for Cardiovascular Research DZHK, Partner Site Rhine-Main, Berlin, Germany.
[3]Goethe University Frankfurt, Faculty of Medicine, Institute for Cardiovascular Physiology, Frankfurt am Main, Germany.
[4]Cardiopulmonary Institute (CPI), 60590 Frankfurt am Main, Germany.
[5]Department of Physiology, Amsterdam Cardiovascular Science, VU University Medical Centre, Amsterdam, The Netherlands.
[6]Max Planck Institute for Heart and Lung Research, Bad Nauheim, Germany.
[7]Goethe University Frankfurt, Faculty of Medicine, Functional Proteomics, Frankfurt am Main, Germany.
[8]Department of Vascular and Endovascular Surgery, Technical University Munich, Munich, Germany.
[9]German Centre for Cardiovascular Research DZHK, Partner Site Munich, Berlin, Germany.
[10]Department of Medicine, Karolinska Institute, Stockholm, Sweden.

† **Corresponding author:** Reinier A. Boon, boon@med.uni-frankfurt.de, Theodor-Stern-Kai 7

60590 Frankfurt am Main, Germany

Total word count: 15,751

Abstract

Background: Vascular aging is characterized by the progressive deterioration of endothelial function. Long non-coding RNAs (lncRNAs) are critical regulators of gene expression and protein function. However, their involvement in aging-related dysregulation of endothelial cell function remains largely unknown. Here, we aim to characterize the aging-regulated lncRNA *MIRIAL* in endothelial cells.

Methods + Results: We initially identified *Mirial* as an aging-induced lncRNA in RNA sequencing data of mouse cardiac endothelial cells. In human umbilical vein endothelial cells (HUVECs), gapmer-mediated knockdown of *MIRIAL* led to decreases in proliferation, migration and basal angiogenic sprouting. Additionally, *MIRIAL* knockdown led to increased mitochondrial mass, spare respiratory capacity, and vascular endothelial growth factor (VEGF)-stimulated sprouting. Mechanistically, we demonstrate that *MIRIAL* forms an *RNA*·DNA:DNA triple helix (triplex) with a regulatory region of the quiescence-promoting Forkhead Box O1 (*FOXO1*) gene, thus inducing its expression. The formation of this triplex involves an *Alu* element within the *MIRIAL* transcript, representing a previously undescribed mechanism of action for a lncRNA. Further, we generated a global *Mirial* knockout mouse line of. Angiogenic sprouting of aortic rings from *Mirial* knockout mice was reduced under basal conditions, but increased after VEGF administration, validating the *in vitro* angiogenic phenotype. Importantly, cardiac contractile function after acute myocardial infarction is severely reduced in *Mirial* knockout mice, as compared to wild-type littermates.

Conclusions: The lncRNA *MIRIAL* is an aging-induced regulator of endothelial quiescence and metabolism.

Key words: Long non-coding RNAs; endothelial cells; aging; quiescence; triple helix

Non-standard abbreviations and acronyms:

AAA	Abdominal aortic aneurysm
AGC	Automatic gain control
AMI	Acute myocardial infarction
AMPK	AMP-activated kinase
ANOVA	Analysis of variance
ASO	Antisense oligonucleotide
ATP	Adenosine triphosphate
BCA	Bicinchoninic acid
BSA	Bovine serum albumin
C. elegans	Caenorhabditis elegans
cDNA	Copy DNA; also: complementary DNA
ChIP	Chromatin immunoprecipitation
CLIP	Crosslinking and immunoprecipitation
CPAT	Coding potential assessment tool
CRISPR/Cas9	Clustered regularly interspaced short palindromic repeats and CRISPR-associated protein 9
Ctrl	Control
CVD	Cardiovascular disease
DAPI	4’,6-diamidino-2-phenylindole
DDX5	DEAD box protein 5
DMEM	Dulbecco’s modified Eagle Medium
DRP1	Dynamin 1-like protein

DTT	Dithiothreitol
EBM	Endothelial basal medium
ECAR	Extracellular acidification rate
ECIS	Electrical cell-substrate impedance sensing
ECL	Enhanced chemiluminescence
EDTA	Ethylenediaminetetraacetic acid
EdU	5-ethynyl-2′-deoxyuridine
EF	Ejection fraction
FACS	Fluorescence activated cell sorting
FBS	Fetal bovine serum
FDR	False discovery rate
FF	Form factor
FITC	Fluorescein isothiocyanate
FOXO1	Forkhead box O1
FUBP3	Far upstream element binding protein 3
FUS	Fused in sarcoma
GAPDH	Glyceraldehyde 3-phosphate dehydrogenase
gRNA	Guide RNA
GSEA	Gene set enrichment analysis
HAS	Human serum albumin
HAT	Histone acetyltransferase
HBSS	Hank’s balanced salt solution
HEK	Human embryonic kidney

HEPES	4-(2-hydroxyethyl)-1-piperazineethanesulfonic acid
HMOX1	Heme oxygenase 1
HUVECs	Human umbilical vein endothelial cells
IBAQ	Intensity-based absolute quantification
ICAM-1	Intercellular adhesion molecule 1
ISHD	Ischemic heart disease
KEGG	Kyoto Encyclopedia of Genes and Genomes
LAD	Left anterior descending
LFQ	Label free quantification
LNA	Locked nucleic acid
lncRNA	Long non-coding RNA
MFC	Mitochondrial fragmentation count
MFF	Mitochondrial fission factor
MIRIAL	MicroRNA-cluster 23a~27a~24-2-associated and Induced by Aging Long non-coding RNA
miRNA	MicroRNA
MORF4L2	Mortality factor 4 like 2
MRPL41	Mitochondrial ribosomal protein L 41
MS	Mass spectrometry
mtDNA	Mitochondrial DNA
MT-ND1	Mitochondrially encoded NADH-ubiquinone oxidoreductase core subunit 1
ncRNA	Non-coding RNA

NTC	Non-targeting control
OCR	Oxygen consumption rate
OPA1	Mitochondrial dynamin like GTPase Optic Atrophy 1
PBS	Phosphate buffered saline
PCR	Polymerase chain reaction
PGAM5	Mitochondrial serine/threonine-protein phosphatase
PGC1β	Peroxisome proliferator-activated receptor gamma coactivator 1-β
PHB (2)	Prohibitin (2)
PRKRA	Protein activator of interferon induced protein kinase
PURA/PURB	Purine-rich element binding protein A/B
qRT-PCR	Quantitative reverse transcription PCR
RELA	NF-κb p65 subunit
REM	Regulatory element
RIPA	Radio-immunoprecipitation assay
ROS	Reactive oxygen species
RPLP0	Ribosomal protein lateral stalk subunit P0
SD	Standard deviation
SDS-PAGE	Sodium dodecyl sulfate-polyacrylamide gel electrophoresis
SEM	Standard error of the mean
SINE	Short interspersed element
siRNA	Small interfering RNA
snoRNA	Small nucleolar RNA
TAF15	TATA-binding protein-associated factor 2N

TBS	Tris-buffered saline
TCEP	Tris(2-carboxyethyl)phosphine
TFR	Triplex forming region
TOMM20	Translocase of outer mitochondrial membrane 20
triplex	*RNA*·DNA:DNA triple helix
VEGF(-A)	Vascular endothelial growth factor (A)
VEGFR2	Vascular endothelial growth factor receptor 2

Introduction

Today, it is well-established that while the majority of the genome is transcribed, only a small fraction of about 1-2% of the genome is protein-coding, whereas the vast majority of the transcriptome is thought to be non-coding [1]. Non-coding RNA (ncRNA) can be roughly categorized into shorter ncRNA – microRNAs (miRNA) are the most well-known example of these – and long noncoding RNAs (lncRNAs). LncRNAs are defined by a length exceeding 200 nucleotides and often exhibit a low abundance per cell. This heterogeneous class of RNA molecules can interact with DNA, other RNAs or proteins, thereby regulating gene expression, as well as RNA and protein function [1-3]. The mechanisms through which lncRNAs can exert their regulatory effects are diverse. Certain lncRNAs can act as epigenetic modifiers in a sequence-specific manner by forming an *RNA*·DNA:DNA triple helix (triplex) with DNA. In this mechanism, a single-stranded lncRNA molecule inserts into the major groove of the DNA double helix *via* Hoogsteen base pairing. This structural arrangement enables the lncRNA to induce alterations in gene expression, thereby influencing cellular processes [4-6]. Several lncRNAs, e.g. *Sarrah* [7], *HOTAIR* [8] and *HIF1α-AS1* [9] have been described to function through this mechanism.

Cardiovascular diseases (CVD) remain the leading cause of mortality worldwide [10]. The predominant risk factor associated with development of CVD is aging [11]. In the vasculature, aging manifests as a gradual decline of endothelial function, stiffening of the vessel wall, compromised angiogenic capacity and increased levels of inflammation [12, 13]. Among the Forkhead Box O (FOXO) transcription factor family, FOXO1 is one of the key members that has been extensively associated with longevity [14-16]. FOXO1 plays a crucial role in promoting endothelial quiescence [14, 17] and is indispensable for endothelial cell homeostasis and

development. Notably, both endothelial loss and overexpression of Foxo1 in mice lead to defects in vasculogenesis, resulting in embryonic lethality [14, 17-19].

We identified an aging-induced lncRNA in murine cardiac endothelial cells that we termed *Mirial* (**Mi**cro**R**NA-cluster 23a~27a~24-2-associated and **I**nduced by **A**ging **L**ong non-coding RNA) (transcript ID: Gm26532, ENSMUSG00000097296), which is previously uncharacterized in endothelial cells. Previous publications have shown *Mirial* expression to be increased in the hippocampi of adult mice after propofol administration, linking lower *Mirial* expression to reduced FoxO signaling [20]. In humans, upregulation of the orthologous lncRNA *MIRIAL* (transcript IDs: LOC284454, AL832183, MIR23AHG, ENSG00000267519 or AC020916.1) has been reported in nasopharyngeal carcinoma [21] and hepatocellular carcinoma [22], and is associated with poorer clinical prognosis. In both conditions, *MIRIAL* appears to exhibit oncogenic properties promoting migration and invasion. Furthermore, Liu et al. described copy number variations of *MIRIAL* in colorectal carcinoma patient samples [23]. A study by Das *et al.* revealed that *MIRIAL* is a stable, single-exonic lncRNA with a half-life of 3 hours. It is polyadenylated, strictly localized to the nucleus and associated with chromatin. Additionally, it has been shown to interact with the RNA helicase DDX5/p68 in HEK293T cells. In contrast to the aforementioned studies of *MIRIAL* in cancer, they proposed its expression to be reduced in various types of cancers and cancer cell lines [24]. Lastly, there is evidence suggesting that *MIRIAL* is upregulated and may serve as diagnostic biomarker in head and neck cancers [25].

Here, we present a comprehensive characterization of the aging-induced lncRNA *MIRIAL* in endothelial cells, where it exerts regulatory control over metabolism and mitochondrial copy number by activating the FOXO1 signaling pathway. FOXO1 plays a pivotal role in repressing

MYC signaling and promoting endothelial quiescence. Concurrent suppression of the p53 signaling pathway leads to enhanced proliferation and angiogenesis. Mechanistically, we discovered that an *Alu* element within the *MIRIAL* transcript forms an *RNA*·DNA:DNA triplex with a regulatory region of the *FOXO1* gene, resulting in its increased expression. Importantly, *MIRIAL* is the first lncRNA harboring an *Alu* element which forms a triplex with genomic DNA. Lastly, we generated a *Mirial* knockout mouse line, which presents with a sensitization of endothelial cells towards VEGF-A signaling in *ex vivo* experiments and a reduced myocardial contractile function after acute myocardial infarction (AMI) *in vivo*.

Materials and Methods

Animals

All mice experiments were carried out in accordance with the principles of laboratory animal care as well as according to the German national laws and the guidelines from Directive 2010/63/EU of the European Parliament on the protection of animals used for scientific purposes. The studies have been approved by the local ethics committee (Regierungspräsidium Darmstadt, Hesse, Germany). Mice were kept in individually ventilated cages (Tecniplast) at 12:12h-light/dark cycles at 21–24°C and 45-60% humidity. Water and ssniff R/M-H complete feed (ssniff Spezialdiäten) were fed *ad libitum*. Young (12 weeks) and aged (72 weeks) wild type C57Bl/6 mice were purchased from Janvier. The *MIRIAL* knockout mouse line was produced on a C57Bl/6N background by Cyagen/Taconic using CRISPR/Cas9 technology according to our requests. Both, male and female animals were used for the experiments. After sacrificing and perfusing the animals with HBSS (Gibco), organs and tissues harvested for RNA or DNA isolation were snap-frozen in liquid nitrogen and later homogenized in QIAzol lysis reagent (QIAGEN) or genomic lysis buffer (Invitrogen), respectively, using the Bead Mill MAX Homogeniser (VWR). The steps of RNA and genomic DNA isolation can be found elsewhere in this manuscript. AMI surgery was performed on 11–13-week-old animals by ligation of the left anterior descending (LAD) coronary artery as described before [26]. Mice were perfused with HBSS (Gibco), and the hearts were harvested 4 weeks after AMI surgery.

Aortic ring assay

Aortic rings were prepared as described before [27]. Aortic rings were fed with fresh growth medium containing VEGF-A (PeproTech) every 2-3 days for 7 days. Then the rings were fixed

with Histofix (Roth), blocked with Protein Block Serum-Free (Dako) and subsequently stained with Isolectin B4 (Vector) and Streptavidin Alexa488 (Invitrogen) and imaged using the Nikon Eclipse Ti2 microscope with 10x magnification and in 5x5 large image mode. Cumulative sprout length was determined using Image J software.

ATP determination assay

Cellular ATP levels were assessed utilizing the Molecular Probes ATP determination kit (Invitrogen). The assay was carried out 48 h after transfection of HUVECs and in accordance with the manufacturer's guidelines. After washing with PBS (Gibco), cells were detached, counted, washed, and resuspended at a concentration of 1,000 cells/µL. Cells were boiled at 95°C for 10 min to achieve cell lysis. Subsequently, the samples were transferred into a white-walled 96-well plate (Greiner) and mixed with the reaction solution supplied with the kit. Luminescence was measured in the samples and an ATP standard curve using the Glomax Multi+ Detection System multiplate reader (Promega).

Caspase assay

24 h after transfection, cells were re-seeded into black-walled 96-well plates (Corning) and caspase activity was determined additional 24 h later using the Apo-ONE Homogeneous Caspase-3/7 kit (Promega) according to the manufacturer’s instructions. Fluorescence was measured using the Glomax Multi+ Detection System plate reader by Promega (excitation 485+/- 20 nm, emission 530 +/- 25 nm).

Cell culture

Pooled HUVECs were purchased from Lonza and cultured in Endothelial Cell Basal Medium (EBM) (Lonza) containing EGM SingleQuots supplements (Lonza) (without ascorbic acid) and

10% fetal bovine serum (FBS) (Gibco). HUVECs were used at passage 2 – 3 for experiments and cell number was determined using the Nucleocounter NC-2000 (Chemometec A/S). Human embryonic kidney (HEK) cell lines (Lenti-X 293T) (Takara) were cultured in high-glucose DMEM (Gibco) with 10 % FBS (Gibco) and 1x Pen/Strep (Roche). Lenti-X 293T cells were kindly provided by the lab of Ralf Brandes/Matthias Leisegang. All cells were regularly tested for mycoplasma contamination and kept at 37°C and 5% CO_2 in a humidified atmosphere.

Chromatin immunoprecipitation

Chromatin immunoprecipitation (ChIP) was performed using the EZ-Magna ChIP G kit (Merck Millipore) following the manufacturer's instructions but with modifications. Briefly, HUVECs were seeded and transfected in 15 cm dishes. 48 h later, cells were washed twice with PBS, scraped off and fixed with formaldehyde (1% final concentration) for 5 min at RT. After three washing steps, nuclear lysates were prepared as described in the kit's instructions. Nuclei were resuspended in 0.2 mL nuclear lysis buffer and DNA was sheared to a length of ~200 – 700 nt using the Bioruptor Plus sonication device (Diagenode) (10 cycles in high setting 30 sec on/30 sec off, followed by 10 cycles in low setting 30 sec on/30 sec off). ChIP was performed as described in the manufacturer's manual using 5 µg of the following antibodies: anti-MORF4L1/2 (Santa Cruz), normal mouse IgG and anti-RNA Polymerase II (both supplied with the kit). DNA was recovered using phenol/chlorophorm/isomylalcohol (1:1:1) (Roth) and eluted in 28 µL DNase free water. Results were obtained by qPCR using primers directed against the *FOXO1* promoter region. The sequences can be found in the Major Resources Table.

CRISPR/Cas9

A dual guide RNA (gRNA) system approach consisting of gRNA-A and gRNA-B was used to remove the triplex-forming region (TFR) of *MIRIAL*. gRNA-A targeted a region upstream of the *Alu* elements harboring the TFR and gRNA-B targeted a region downstream of them. The design of the gRNA was based on the web-interface of CRISPOR (http://crispor.tefor.net/) [28].

The gRNAs were cloned into a lentiCRISPRv2 vector backbone via Esp3I as described in [29]. lentiCRISPRv2 was a gift from Feng Zhang (Addgene plasmid #52961; http://n2t.net/addgene:52961; RRID:Addgene_52961) [29]. The modification of the lentiCRISPRv2 plasmid with hygromycin resistance was provided by Frank Schnütgen (Dept. of Medicine, Hematology/Oncology, University Hospital Frankfurt, Goethe University, Frankfurt, Germany).

For annealing, the following oligonucleotides were used: *MIRIAL* TFR: gRNA-A: 5'-CAC CGA CCC AGA AGG GAC ACA AGC-3' and 5'-AAA CGC TTG TGT CCC TTC TGG GTC C-3'; gRNA-B 5'-CAC CGC CCA TCT GAT TTC AAG ATA G-3' and 5'-AAA CCT ATC TTG AAA TCA GAT GGG C-3'. gRNA-A was cloned into lentiCRISPRv2 with puromycin resistance, gRNA-B was cloned into lentiCRISPRv2 with hygromycin resistance. After cloning, the gRNA-containing lentiCRISPRv2 vectors were sequenced and purified.

Lentivirus production was performed by transfecting Lenti-X 293T cells (632180, Takara) with GeneJuice Transfection Reagent (70967, Merck), packaging plasmid psPAX2, and the envelope plasmid pVSVG (pMD2.G). psPAX2 and pMD2.G were a gift from Didier Trono (12260, Addgene plasmid, http://n2t.net/addgene:12260; RRID:Addgene_12260 and 12259, http://n2t.net/addgene:12259; RRID:Addgene_12259, respectively). Non-targeting control (NTC) vectors were used as controls.

Viral supernatants were harvested 48 h and 72 h post-transfection, concentrated (Lenti-X Concentrator, Takara) and incubated with HUVECs (p3) in the presence of polybrene (8 µg/mL, Sigma) overnight, followed by expansion and selection (Puromycin 1 µg/mL, Sigma, Hygromycin 100 µg/mL, Merck Millipore). Cells were harvested 10 days post-transduction and total RNA, and genomic DNA were isolated as described elsewhere in this manuscript.

Validation of the CRISPR/Cas9 knockout of the *MIRIAL* TFR was performed from genomic DNA. The CRISPR/Cas9 target site was amplified by PCR using 2x Rapid Taq Master Mix (Vazyme Biotech) containing forward and reverse primers (10 µM each) and 10 ng purified DNA followed by electrophoresis on an agarose gel stained with Midori Green (Nippon Genetics). The following primers were used: *MIRIAL* TFR KO: 5'- ACT CCT GGC TTC CGG TAT CA -3' and 5'- AGG CAG GGA GGA TCA GCT ATT -3'; *GAPDH*: 5'- TGG TGT CAG GTT ATG CTG GGC CAG -3' and 5'- GTG GGA TGG GAG GGT GCT GAA CAC -3'.

Echocardiography

Echocardiography was performed to assess cardiac contractile function one, 14 and 28 days after AMI surgery using a Vevo 3100 imaging system (VisualSonics).

ECIS

Electrical Cell-substrate Impedance Sensing (ECIS) was performed to assess endothelial barrier integrity and migration after wounding of an endothelial monolayer as described before [30].

Flow cytometry

Flow cytometry was used to measure cell cycle progression (Click-iT EdU Flow Cytometry Assay Kit and FxCycle Violet, both Thermo Fisher), DNA damage (anti-H2AX(pS139)-PE, BD

Biosciences), mitochondrial mass (Mitotracker Green, Thermo Fisher), mitochondrial membrane potential (TMRM, Thermo Fisher) and reactive oxygen species (ROS) production (MitoSOX, invitrogen) following manufacturer's instructions. Briefly, cells were transfected as described earlier, incubated with the respective labelling compound or antibody for 10-60 min, washed, fixed and permeabilized if required, detached using 0.5% trypsin/EDTA (Gibco), transferred to FACS tubes (BD Biosciences) and then mean fluorescence was measured using the FACS Canto II flow cytometer (BD Biosciences). For viability exclusion cells were stained using either DAPI (Thermo Fisher) or the LIVE/DEAD Fixable Far Red Dead Cell Stain Kit (Thermo Fisher) according to manufacturer's instructions. Unlabeled cells were used as negative control. λ excitation/emission: DAPI 405/450 nm, EdU 488/530 nm, FxCycle Violet 405/450 nm, γH2A.X-PE 488/576 nm, LIVE/DEAD 633/660 nm, MitoSOX 510/580 nm, MitoTracker Green 490/516 nm, TMRM 488/573 nm.

Genomic DNA isolation

Isolation of genomic DNA was performed using the PureLink Genomic DNA Mini Kit by Invitrogen according to the manufacturer's instructions. Purified genomic DNA was eluted in a volume of 100 µL of Genomic Elution Buffer (provided with the kit). Concentration of purified genomic DNA was determined using the nanodrop2000 spectrophotometer (Thermo Scientific), diluted to 2.5 ng/µL and then submitted to qRT-PCR. To determine mtDNA content relative to nuclear DNA, we used MT-ND1 and RPLP0 primers, respectively. To determine telomere length, we used telomere-specific primers and 36B4D (single copy gene) primers as reference as described in [31].

Growth curve

Cells were seeded in 24-well plates (Greiner), transfected and the cell number was assessed at 0 h, 24 h, 48 h and 72 h post-transfection or only at 0 h and 72 h post-transfection using C-Chip Neubauer Improved disposable hemocytometers (NanoEntek).

Histology

Mouse hearts were fixed overnight in 4% PBS-buffered formaldehyde (Histofix, Roth) and subsequently embedded in paraffin. The staining of mouse heart sections with Sirius Red (fibrosis) was carried out as detailed in another study [26]. Infarct size was determined by calculating the ratio of the infarct's length to the circumference of the left ventricle as described before [32]. Fibrosis was assessed by dividing the Sirius red-positive area by the total area of each section. These measurements were performed across three consecutive sections of the hearts.

Immunoblotting

Cells were washed with ice-cold PBS (Gibco) and lyzed for 1 h in Radio-Immunoprecipitation Assay (RIPA) buffer (Thermo Scientific) containing 1x protease and phosphatase inhibitors (Halt Protease Inhibitor Cocktail 100×, Thermo Scientific). After centrifugation (10 min, 10,000x *g*), the protein concentration of the supernatant was determined using the Pierce BCA Protein Assay Kit (Thermo Scientific) and equal amounts of protein were boiled in 4x Laemmli Sample Buffer (Bio-Rad) containing β-mercaptoethanol (AppliChem). Samples were separated by SDS-PAGE using Mini-PROTEAN TGX Gels 4-15% (Biorad) and 1x Laemmli Buffer for SDS-PAGE (Serva) and then transferred to Nitrocellulose membrane (Invitrogen) by wet-tank blotting. Membranes were blocked with either 5% non-fat dry powdered milk (Roth) or

5% BSA (AppliChem) in 1x TBS + 0.1% Tween20 (both from Roth). Primary antibodies (Cell Signaling or Novus Bio) are incubated in blocking buffer overnight at 4°C. Secondary antibodies (Agilent Dako) were incubated in TBS-T for 1 h at room temperature. For details on all antibodies please see the Major Resources Table in the Supplemental Materials. Signal was detected using the Pierce ECL Western Blotting Substrate by Thermo Scientific and the ChemiDoc Touch Imaging System (Biorad). Intensities were measured using Image Lab Software (Biorad) and normalized to the housekeeping proteins GAPDH, β-Tubulin or Vinculin.

Immunohistochemistry

Sections for immunohistochemistry were prepared as described before [33] including the antigen retrieval step. Capillary density was visualized using the following primary and secondary antibodies: Isolectin B4 (Vector) and Streptavidin Alexa488 (Invitrogen), wheat germ agglutinin Alexa647 (Thermo Fisher), anti-actin alpha smooth muscle Cy3 (Sigma) and Hoechst 33342 (Anaspec). Slides were mounted using Fluoromount-G mounting medium (Thermo Fisher). Sections were imaged using the Zeiss LSM 780 confocal microscope equipped with a 40x objective and analyzed using Volocity software 6.5.1 (Quorum Technologies).

KEGG pathway analysis

The web tool DAVID 6.8 (https://david.ncifcrf.gov/) [34, 35] was used for Kyoto Encyclopedia of Genes and Genomes (KEGG) pathway analysis using the parameters fold change ≥ 1.5 and $p \leq 0.05$.

miRNA expression levels

microRNA expression levels were determined using TaqMan assay system by Applied Biosystems. Briefly, samples were reversely transcribed individually for each target miRNA, including U6 snoRNA as a reference using the TaqMan MicroRNA Reverse Transcription Kit. cDNA was then subjected to qRT-PCR using TaqMan MicroRNA Assay probes and TaqMan Fast Advanced Master Mix.

Mitochondrial structure analysis

Assessment of mitochondrial fragmentation was performed on confluent HUVECs seeded on 8-well format Ibidi µ-slides following transfection with gapmeR control or gapmeR targeting the lncRNA *MIRIAL*. The cells were subsequently washed and fixed with 4% paraformaldehyde for 10 min at room temperature. Subsequently, HUVECs were permeabilized with 0.2% triton X-100, followed by blocking with 1% human serum albumin (HSA). Mitochondria were stained using rabbit monoclonal TOMM20 antibody 1:100 (Santa Cruz, SC-11415) in 1% HSA for 1 h at 37°C followed by an incubation with FITC-conjugated secondary goat anti-rabbit IgG antibody 1:100 (Thermo Fisher, Alexa Fluor 488, A32731) for 1 h at 37°C. Cells were washed three times with 0.1% HSA and four drops of mounting medium were added into the well. The cells were imaged on a Nikon Eclipse T*i*2-E inverted fluorescence microscope (Nikon Instruments Inc., USA) with a 40X objective.

Mitochondrial structure was quantified as described before [36-39] . Briefly, images were opened in FIJI and were adjusted to optimize visualization of the mitochondria (five visual fields were acquired and at least 100 cells were analyzed per condition per experiment; *n*=3 independent experiments). The images were then converted to a binary image and the polygon selection tool was used to outline cells. After selecting the cell, the Analyze Particles function (pixel size

10-infinity; circularity 0.00-1.00) was used to count the number of noncontiguous discrete particles. For every condition, ~100 cells per experiment were analyzed to calculate the mitochondrial fragmentation count (MFC) and form factor (FF) values. MFC is assigned by dividing the number of mitochondrial segments in the cell by the total mitochondrial mass and multiplied by 1000. FF is calculated as (perimeter^2/4.π.area).

Prediction of triplex formation by *MIRIAL*

Potential *RNA*·DNA:DNA triplex formation by *MIRIAL* was predicted using *TriplexAligner* (v1.0) [40]. Briefly, the transcript sequence of *MIRIAL* was used as the RNA input to the algorithm, with the DNA input being made up of promoter or regulatory element sequences. Promoter sequences were defined as being 3500 base pairs upstream and 500 base pairs downstream of transcription start sites as annotated in the R package *TxDb.Hsapiens.UCSC.hg38.knownGene*. The regulatory elements used were taken from *EpiRegio* [41]. *TriplexAligner* predicts triplex formation between RNA and DNA sequences using local alignment with probabilistic scoring matrices learned from triplex-sequencing data. The predicted triplex-forming region of *MIRIAL* was determined by summing the *TriplexAligner* – $\log_{10}(E)$ values obtained across every predicted interaction at base-pair resolution along the length of the transcript. Predicted target sites of *MIRIAL* were further stratified by H3K27ac ChIP-sequencing signal from *ENCODE* [42] (accession ENCFF343KDE, available at s3://encode-public/2020/09/30/aa0c90aa-3f77-4806-8cb1-d98c71c411f6/ENCFF343KDE.bigWig).
H3K27ac signal was summed per genomic feature (promoter or REM) and used to identify candidate *MIRIAL* triplex target sites of regulatory importance. Total H3K27ac signal in the feature was multiplied by the *TriplexAligner* $-\log_{10}(E)$ value for the predicted interaction between *MIRIAL* and the respective DNA region to produce a combined score. The logarithm

of this score was then rescaled to between 0 and 1 to produce a combined score used to stratify the genomic features.

RNA affinity purification followed by mass spectrometry

Nuclear fractions from untransfected HUVECs were prepared using cytoplasmic lysis buffer (10 mM Tris/HCl pH 7.5, 150 mM NaCl, 0.15% (v/v) NP-40), sucrose buffer (10 mM Tris/HCl pH 7.5, 150 mM NaCl, 24% (w/v) sucrose), glycerol buffer (20 mM Tris/HCl pH 7.9, 75 mM NaCl, 0.5 mM EDTA, 0.85 mM DTT, 50% (v/v) glycerol) and nuclei lysis buffer (10 mM HEPES pH 7.6, 7.5 mM $MgCl_2$, 0.2 mM EDTA, 0.3 M NaCl, 1 M urea, 1% (v/v) NP-40, 1mM DTT). The nuclear lysates were adjusted to 150 mM NaCl, 160 U RNase inhibitor, 1 mM DTT, and 1x Protease inhibitor in 1x RNase H buffer (New England Biolabs). For RNA pulldown 200 pmol of biotinylated ASOs directed against *MIRIAL* were incubated overnight at 4°C with pre-cleared (2 h, 4°C) nuclear lysates. The next day, ASO-protein-complexes were captured from the lysate by adding pre-blocked (yeast tRNA and glycogen, 0.2 mg/mL each) and washed (Washing buffer: 50 mM Tris/HCl; pH 8.0, 150 mM NaCl, 1 mM EDTA, 0.05% (v/v) NP-40 and 1x protease inhibitor) magnetic Streptavidin beads (DynaBeads MyOne StreptAvidin C1, Invitrogen) and incubating them for 1 h at 37°C. The beads were then washed (mild washing buffer: 20 mM Tris/HCl; pH 8.0, 10 mM NaCl, 1 mM EDTA, 0.05% (v/v) NP-40 and 1x Protease inhibitor) and eluted using 10 mM d-Biotin in mass spec buffer (10 mM Tris/HCl; pH 8.0, 50 mM NaCl) for 30 min at 37°C and 500 rpm. Parts of the elution fraction were held back for RNA extraction and silver staining. The rest was snap-frozen in liquid nitrogen and then submitted to mass spectrometry.

Eluates from the RNA affinity purification experiments were supplemented with 2 M GdmCl, 50 mM Tris/HCl pH 8.5, 10 mM TCEP and incubated at 95°C for 5 min. Reduced thiols were

alkylated with 40 mM chloroacetamid and samples were diluted with 25 mM Tris/HCl pH 8.5, 10% acetonitrile to obtain a final GdmCl concentration of 0.6 M. Proteins were digested with 1 µg trypsin (sequencing grade, Promega) overnight at 37°C under gentle agitation. Digestion was stopped by adding trifluoroacetic acid to a final concentration of 0.5%. Peptides were loaded on multi-stop-and-go tip (StageTip) containing six C18-disks. Purification and elution of peptides was performed as described in Rappsilber and Mann (2007). Peptides were eluted in wells of microtiter plates, dried and resolved in 1% acetonitrile, 0.1% formic acid. Liquid chromatography / mass spectrometry (LC/MS) was performed on Thermo Scientific™ Q Exactive Plus equipped with an ultra-high performance liquid chromatography unit (Thermo Scientific Dionex Ultimate 3000) and a Nanospray Flex Ion-Source (Thermo Scientific). Peptides were loaded on a C18 reversed-phase pre-column (Thermo Scientific) followed by separation on a with 2.4 µm Reprosil C18 resin (Dr. Maisch GmbH) in-house packed picotip emitter tip (diameter 100 µm, 15 cm from New Objectives) using a gradient from 4% acetonitrile, 0.1% formic acid to 40% eluent B (99% acetonitrile, 0.1% formic acid) for 30 min and a second gradient to 60% B for 5 min with a flow rate 300 nL/min. MS data were recorded by data dependent acquisition. The full MS scan range was 300 to 2000 m/z with resolution of 70,000, and an automatic gain control (AGC) value of 3*E6 total ion counts with a maximal ion injection time of 160 ms. Only higher charged ions (2+) were selected for MS/MS scans with a resolution of 17,500, an isolation window of 2 m/z and an automatic gain control value set to 1*E5 ions with a maximal ion injection time of 150 ms. MS1-Data were acquired in profile mode. MS Data were analyzed by MaxQuant (v1.6.1.0) [19029910] using default settings. Proteins were identified using reviewed human reference proteome database UniProtKB with 71785 entries, released in 2/2018. The enzyme specificity was set to Trypsin. Acetylation (+42.01) at N-terminus and oxidation of methionine (+15.99) were selected as

variable modifications and carbamidomethylation (+57.02) as fixed modification on cysteines. False discovery rate (FDR) for the identification protein and peptides was 1%. Label free quantification (LFQ) and intensity-based absolute quantification (IBAQ) values were recorded. Data were further analyzed by Perseus (v. 1.6.1.3). Contaminants and reversed identification were removed. Protein identification with at least 4 valid quantification values in at least one group were further analyzed. Missing values were replaced by background values from normal distribution. Student´s t-test was used to identify significantly enriched proteins between experimental groups.

RNA immunoprecipitation

For RNA immunoprecipitation, 5 µg of antibodies (p53 (1C12) (Cell Signaling) or MORF4L1/2 (Santa Cruz) and Normal Mouse IgG (Santa Cruz)) were used. Briefly, HUVECs cultured on 150mm-dishes (Greiner) until confluency, crosslinked with 50 mJ/cm^2 UV light, lyzed in lysis buffer (50 mM Tris/HCl pH 8.0, 150 mM NaCl, 0.5% NP40, 1 mM EDTA, protease inhibitors) and incubated overnight with washed antibody-coated magnetic protein G beads (Dynabeads, invitrogen) in lysis buffer without NP40. Beads were then washed with binding buffer (50 mM Tris/HCl pH 8.0, 150 mM NaCl, 0.05% NP40, 1mM EDTA), eluted by proteinase K digest (New England Biolabs) and RNA was recovered using phenol/chloroform/isoamylalcohol (1:1:1) (Roth). 5% of the input and the elution fractions were held back, boiled in 4x Laemmli Sample Buffer (Bio-Rad) containing β-mercaptoethanol (AppliChem) and used for subsequent SDS-PAGE and immunoblotting.

RNA interference & miRNA overexpression

HUVECs were cultured at 50-60% confluency before being transfected with siRNA (QIAGEN or Sigma), LNA GapmeRs (QIAGEN) or pre-miRs (ambion) according to manufacturer's

recommendations using Lipofectamine RNAiMax (Invitrogen) and serum reduced OptiMEM (Gibco). LNA control A (QIAGEN), siRNA directed against Firefly Luciferase (siCtrl) (Sigma) or pre-miR negative control (ambion) were transfected as controls. For concentrations and sequences of antisense oligonucleotides (ASOs) and miRNA precursors please see the Major Resources Table in the Supplemental Materials. 4 h after transfection the medium was changed to full endothelial growth medium.

RNA-sequencing

HUVECs were transfected with either LNA Control or LNA MIRIAL. 48 h post-transfection, RNA was isolated as described earlier. RNA quality control, library preparation, RNA-sequencing and analysis was performed as described in 30. The related data are available on Gene Expression Omnibus (accession number GSE248795; reviewer token: cxutusselbenlkp; https://www.ncbi.nlm.nih.gov/geo/query/acc.cgi?acc=GSE248795). Human aneurysmal abdominal arteries were harvested during OR in the Department of Vascular and Endovascular Surgery at the Klinikum rechts der Isar of the Technical University Munich and previously published [43]. Single-cell RNA sequencing and analysis were performed as described [43]. The related data are available on Gene Expression Omnibus (accession number GSE237230). RNA-sequencing data of cardiac endothelial cells derived from young and aged mice was published previously and is available online [44].

Seahorse

48 h prior to the assay, HUVECS were transfected with either LNA Control or LNA *MIRIAL*. 24 h after the transfection, cells were re-seeded into Seahorse XF96 Cell Culture Microplates (Agilent) coated with fibronectin and gelatin. The Seahorse XF Glycolysis Stress Test and Seahorse XF Cell Mito Stress Test were performed using the same-named kits and the

Seahorse XFe96 Analyzer (all by Agilent) following the manufacturer's instructions. Cells were assayed in Seahorse XF Base Medium (Agilent) containing L-glutamine, D-glucose, and sodium pyruvate (all from Sigma), pH 7.4. Oxygen consumption rate (OCR) and extracellular acidification rate (ECAR) were normalized to cell number per well determined by Hoechst 33258 staining after the assay. Fluorescence was measured using the Glomax Multi+ Detection System plate reader by Promega (fluorescence: excitation 365 nm, emission 410-460 nm; absorption: 560 nm).

Senescence-associated β-galactosidase staining

Cellular senescence was assessed using the Senescence Associated β-Galactosidase Staining kit (Cell Signaling) 48 hours post-transfection. Cells were washed twice with PBS (Gibco) and fixed for 5 minutes at room temperature using 1x fixative solution (20% formaldehyde, 2% glutaraldehyde in PBS). After three washes with PBS (Gibco), cells were incubated with staining solution containing the chromogenic substrate 5-bromo-4-chloro-3-indolyl-β-D-galactopyranoside (X-Gal) (pH adjusted to pH 6.0 with HCl) overnight at 37°C without CO_2 in a non-humidified incubator. Images were captured at 5x magnification using a Zeiss Axiovert 100.

Sequence homology alignment

Sequence alignment of human and mouse *MIRIAL/Mirial* was performed as described in [7]. The LALIGN DNA:DNA tool of the FASTA Sequence Comparison software (University of Virginia) was used with default parameters [45].

Spheroid sprouting assay

HUVECs were transfected with either LNA Control or LNA *MIRIAL*. The next day, 400 cells per well are re-seeded in semi-solid medium (80% EBM + 20% methylcellulose (0.6 g/L, Sigma)) in 96-well U-bottom plates (Greiner) to form three-dimensional spheroids. After additional 24 h, the spheroids were carefully harvested, centrifuged, re-suspended in a mixture of 80% methocoel and 20% FBS (Gibco) and then re-seeded in a collagen medium (10x M199 (Sigma), collagen stock solution type I (Corning), HEPES, NaOH (both Sigma). After a 30 min incubation at 37°C, the embedded spheroids are stimulated with VEGF-A (PeproTech) at a final concentration of 50 ng/mL in endothelial growth medium. Unstimulated spheroids fed with only endothelial growth medium were included as controls. 24 h later, spheroids were fixed with HistoFix (Roth) for 30 min and imaged using the Zeiss AxioVert microscope with 10x magnification. Cumulative sprout length was quantified using Image J software.

Subcellular fractionation

Cytoplasmic, nucleoplasmic and chromatin fractions of untransfected HUVECs were isolated as described in [30].

Total RNA isolation, cDNA synthesis and qRT-PCR

Total RNA was isolated using QIAzol lysis reagent (QIAGEN) and the Direct-zol RNA MiniPrep Kit (Zymo Research) (for HUVEC samples) including recommended DNase-I digestion, or the miRNeasy Micro Kit or Mini Kits (QIAGEN) (for in vivo samples) following the manufacturer's instructions. RNA was reversely transcribed to cDNA using random hexamer primers (QIAGEN) and MultiScribe Reverse Transcriptase (Invitrogen). qRT-PCR was performed using Fast SYBR Green Master Mix (Applied Biosystems) and either Step One Plus or ViiA 7 thermocyclers (Applied Biosystems). For primer sequences please see the Major Resources Table in the Supplemental Materials. Gene expression was normalized to Ribosomal protein

lateral stalk subunit P0 (*RPLP0*) or glyceraldehyde-3-phosphate dehydrogenase (*GAPDH*) expression. Gene expression levels were analyzed using the $2^{-\Delta CT}$ method.

Statistics

Statistical analysis was performed using GraphPad Prism 7.02, 8.0.1 or 9.0.2 for Windows (GraphPad Software, www.graphpad.com). Results are presented as mean ± standard deviation (SD) or standard error of the mean (SEM). Gaussian distribution was assessed using the Shapiro-Wilk normality test. To compare two conditions, paired or unpaired student's *t* test, Mann-Whitney test or Kolmogorov-Smirnov tests were used. To compare multiple conditions, we used (Brown-Forsythe and Welch) analysis of variance (ANOVA) or Kruskal-Wallis test with Tukey *post-hoc* test.

Results

MIRIAL is an aging-induced long non-coding RNA that regulates endothelial cell quiescence

Mirial (transcript ID: Gm26532) was first identified in an RNA-sequencing data set generated from cardiac endothelial cells of 12 weeks old and 20 months old mice **(Fig. 1A)** [44]. These data showed that *Mirial* was upregulated during aging, which was further confirmed in aortic intima samples of young (12 weeks) and aged (20 months) mice analyzed by qRT-PCR **(Fig. 1B)**. The *Mirial* gene locus also encompasses the miRNA cluster 23a-27a-24-2 and is highly conserved. By analyzing the corresponding locus in humans, the human orthologue of *Mirial* could be identified **(Supp. Fig. 1A)**. Interestingly, *MIRIAL* was also found to be upregulated in an RNA-sequencing data set of human native endothelial cells obtained from both young and aged individuals [46]. Previously, it had been shown that *MIRIAL* is highly sequence conserved solely in primates [24]. To assess the degree of sequence conservation between human and mouse we employed the LALIGN DNA:DNA tool [47], which revealed that around 50% of the mouse sequence is also present in the human orthologue **(Supp. Fig. 1B)**. Comparing the coding probability of *MIRIAL* with known transcripts using the Coding-Potential Assessment Tool (CPAT) [48] we found that *MIRIAL* exhibited a coding probability similar to well-known lncRNAs such as *XIST* and *MALAT1*. Conversely, protein-coding transcripts like *GAPDH*, but also *ZSWIM4*, the protein-coding gene upstream in the locus of *MIRIAL*, were found on the opposite side of the spectrum **(Supp. Fig. 1C)**. By performing RNA-sequencing analyses, we assessed the transcription levels of *MIRIAL* in various human cell types of cardiovascular origin. The results demonstrated that *MIRIAL* is expressed in endothelial cells of different vascular beds, as well as in other non-endothelial cell types including cardiomyocytes **(Supp. Fig. 1D)**. In the context of cardiovascular disease, *MIRIAL* expression was induced in cardiac

biopsy samples from patients with ischemic heart disease (ISHD) **(Fig. 1C)** and in endothelial cells from human abdominal aortic aneurysm (AAA) samples using single-cell RNA-sequencing **(Supp. Fig. 1E)** [43]. To investigate the function of *MIRIAL*, we chose a loss-of-function approach using LNA gapmers in human umbilical vein endothelial cells (HUVECs), achieving a knockdown efficiency of approximately 80-88% **(Supp. Fig. 2A)**. *MIRIAL* silencing resulted in a decrease in proliferation **(Fig. 1D)** with a block of the cell cycle at the G0/G1 phase **(Fig. 1E)**. A scratch-wound assay combined with electric cell-substrate impedance sensing (ECIS) showed reduced barrier function **(Supp. Fig. 2B)** and impaired migration **(Fig. 1F)** after *MIRIAL* knockdown. Next, we assessed whether these effects were due to quiescence (a reversible reduction in cellular activity), senescence or apoptosis (both of which are irreversible). Apoptosis was unchanged in *MIRIAL* knockdown cells, as assessed by Caspase-3/-7 activity measurement **(Fig. 1G)**. In addition, there was no change in number of senescent cells after *MIRIAL* knockdown using a senescence-associated β-galactosidase staining **(Supp. Fig. 2C)**, DNA-damage-associated y-H2A.X staining **(Supp. Fig. 2D)** or telomere length measured by qPCR **(Supp. Fig. 2E)**. These results suggested that loss of *MIRIAL* induces quiescence rather than senescence or apoptosis. Given the observed decrease in proliferation and migration, we hypothesized that angiogenic sprouting would also be reduced. This was confirmed using a spheroid sprouting assay under unstimulated conditions. Importantly, stimulation with VEGF-A resulted in an increase in angiogenic sprouting when *MIRIAL* was silenced, as compared to VEGF-A stimulated control cells **(Fig. 1H)**. Moreover, VEGF-A stimulation rescued the effects of *MIRIAL* knockdown on proliferation **(Supp. Fig. 2F)**. Taken together, these results suggest that loss of *MIRIAL* induces a reversible state of quiescence of endothelial cells.

***MIRIAL* regulates endothelial mitochondrial metabolism**

Glycolysis serves as the predominant pathway for energy production in endothelial cells, and the rate of glycolysis determines endothelial quiescence [49, 50]. To investigate the potential impact of *MIRIAL* on energy homeostasis in endothelial cells, we used the Seahorse glycolysis stress test. Surprisingly, *MIRIAL* knockdown did not affect glycolysis **(Supp. Fig. 3A and 3B)**. However, using the mitochondrial stress test, we found that *MIRIAL* knockdown led to an increase in maximal respiration **(Fig. 2A and 2B)** and spare respiratory capacity (SRC) **(Fig. 2C)**, while basal respiration remained unchanged **(Fig. 2A and 2B)**. Furthermore, ATP production **(Fig. 2D)** and cellular ATP levels were increased **(Fig. 2E)** after *MIRIAL* knockdown. To determine the underlying cause of this apparent increase in mitochondrial activity, we analyzed mitochondrial content after knockdown of *MIRIAL*. We found an increase in mitochondrial mass **(Fig. 2F)** and mitochondrial DNA content **(Fig. 2G)** relative to nuclear DNA following *MIRIAL* knockdown. Nevertheless, mitochondrial membrane potential **(Supp. Fig. 3C)** and production of reactive oxygen species (ROS) **(Supp. Fig. 3D)** remained unchanged, suggesting that *MIRIAL* silencing induces the number of functional mitochondria.

The tightly regulated processes of fission and fusion play pivotal roles in maintaining the cellular oxidative capacity, energy supply and biomass supply through coordinating mitochondrial copy number [51]. Accordingly, we wanted to explore whether these processes are involved in the mechanism by which *MIRIAL* knockdown augments mitochondrial copy number. Consistent with the increase of total mitochondrial mass and mitochondrial DNA content after knockdown of *MIRIAL*, we also found an elevation in the expression levels of almost all key players relevant for fission and fusion, including mitochondrial fission factor (MFF), dynamin 1-like protein (DRP1), Mitofusin-1, Mitofusin-2, mitochondrial dynamin like GTPase Optic Atrophy 1 (OPA1) **(Supp. Fig. 4 A-G)** and the transporter of the outer mitochondrial membrane (TOMM20) **(Supp. Fig. 4H)**, responsible for mitochondrial

membrane transport. To investigate the impact of increased levels of fission and fusion proteins on mitochondrial morphology following *MIRIAL* knockdown, we utilized TOMM20 staining followed by immunofluorescence microscopy **(Fig. 2H)**. We quantified the mitochondrial fragmentation count (MFC), aspect ratio (a measure of mitochondrial length and structural integrity), and form factor (a combined measure of mitochondrial elongation and branching). Our results showed a significant increase in the fragmentation count **(Fig. 2I)** and a reduction in the form factor **(Fig. 2J)** upon *MIRIAL* knockdown. However, the aspect ratio remained unchanged **(Fig. 2K)**. These findings suggest that the loss of *MIRIAL* increases mitochondrial content and function, but this effect does not seem to be mediated through changes in fission or fusion. The increased fragmentation count observed after *MIRIAL* silencing indicates a higher number of mitochondria. These mitochondria exhibit less branching, yet their individual structural integrity and length remain unaltered. In summary, these results show that knockdown of *MIRIAL* heightens functional mitochondrial content in endothelial cells.

***MIRIAL* knockdown in HUVECs activates the p53 signaling pathway**

To gain insight into the role of *MIRIAL* in endothelial cell quiescence, we first focused on its subcellular localization. Subcellular fractionation of HUVECs into cytoplasmic, nucleoplasmic and chromatin fractions revealed that *MIRIAL* was predominantly present in the nucleus (~80%), with a significant proportion present in the chromatin fraction **(Supp. Fig. 4I)**. Given this localization pattern, we hypothesized that *MIRIAL* might directly regulate gene expression. To assess its impact on gene expression we performed RNA-sequencing of HUVECs after *MIRIAL* knockdown, comparing them to control-transfected cells. Following *MIRIAL* knockdown, 974 genes were differentially expressed (Adjusted p-value < 0.01,

absolute $\log_2$(fold change) > 0.585) **(Fig. 3A)**. Kyoto Encyclopedia of Genes and Genomes (KEGG) pathway enrichment analysis demonstrated that genes associated with the cell cycle were downregulated significantly **(Fig. 3B)**, aligning with our previous findings on cell proliferation **(Fig. 1C)**. In addition, we observed a significant upregulation in genes annotated as members of the p53 signaling pathway **(Fig. 3B)**.

Under basal conditions, p53 is constantly expressed and subsequently poly-ubiquitinylated by the E3 ubiquitin-protein ligase MDM2, leading to its proteasomal degradation. However, in response to various stressors, such as irradiation, DNA damage, metabolic or oxidative stress, p53 undergoes phosphorylation at multiple sites, resulting in its stabilization and nuclear translocation. In the nucleus, p53 acts as a transcription factor regulating the expression of various genes [52]. We validated the activation of p53 target genes using qRT-PCR, showing that *MIRIAL* knockdown indeed induces expression of typical p53 target genes (*HMOX1*, *LIF*, *CYFIP2*, *CMBL*, *GDF15*, *CDKN1A*, and *RRM2B*). Importantly, the upregulation of p53 target genes was fully dependent on the presence of p53, since knockdown of p53 using siRNA, rescued the loss-of-*MIRIAL*-mediated induction of these target genes **(Fig. 3C)**. In addition, we confirmed the upregulation of p21 (*CDKN1A*) **(Fig. 3D)**, p53 **(Fig. 3E)** and phosphorylation of p53 at Ser15 **(Fig. 3F)** on the protein level and discovered a physical interaction between p53 and *MIRIAL* using crosslinking and RNA immunoprecipitation (CLIP) **(Fig. 3G)**. Interestingly, the increase in mitochondrial DNA in *MIRIAL* knockdown cells could not be rescued by a simultaneous knockdown of p53 **(Fig. 3H)**, indicating that p53 induction is not responsible for the observed increase in mitochondrial activity following *MIRIAL* silencing.

The primary transcript of the *MIRIAL* locus which contains both the miRNAs and *MIRIAL* is immediately cleaved by Drosha after transcription [24]. Given the mutual transcription of the

miRNAs and *MIRIAL*, it was essential to investigate whether a potential decrease in miRNA abundance contributed to the phenotype. Using TaqMan miRNA assay probes, we assessed the expression levels of all three members of the miRNA cluster (miR-23a, miR-27a and miR-24-2) after *MIRIAL* knockdown. All three miRNAs were downregulated following *MIRIAL* knockdown **(Supp. Fig. 5A)**. If this reduction were functionally relevant, we would expect an upregulation of the target genes regulated by these miRNAs. However, expression levels of two selected target genes of each miRNA did not increase after *MIRIAL* knockdown **(Supp. Fig. 5B)**, suggesting that the moderate reduction in miRNA expression did not result in target de-repression. Nonetheless, to exclude the possibility that the observed phenotype resulting from silencing of *MIRIAL* is due to reduction of these miRNAs, we performed miRNA overexpression experiments by transfecting HUVECs with combined pre-miRNAs achieving expression levels 40-150-fold higher than control **(Supp. Fig. 5C)**. Notably, *MIRIAL* knockdown efficiency was not affected by miRNA overexpression **(Supp. Fig. 5D)**. We further assessed whether miRNA overexpression could rescue the functional effects of *MIRIAL* knockdown on cell proliferation, mitochondrial DNA content and p53 target gene expression. While miRNA overexpression increased proliferation, this effect was independent of *MIRIAL*, as knockdown of *MIRIAL* still significantly decreased cell numbers **(Supp. Fig. 5E)**. Additionally, mitochondrial DNA content remained elevated after *MIRIAL* knockdown, despite overexpression of the miRNAs **(Supp. Fig. 5F)**. Regarding p53 target gene expression, we observed that *HMOX1*, *RRM2B* and *MDM2* were the only genes influenced by miRNA overexpression, with *HMOX1* being a known target of miR-24 [53] **(Supp. Fig. 5G)**. These findings strongly suggest that the effects of *MIRIAL* silencing on endothelial cells are unlikely to be solely attributed to a reduction in miR-23a, miR-27a and miR-24-2 expression.

In conclusion, the results from these loss-of-function experiments provide evidence that *MIRIAL* acts as a repressor of p53 signaling and interacts with p53. However, this pathway does not contribute to the *MIRIAL*-mediated reduction of mitochondrial content. Furthermore, the effects of *MIRIAL* silencing on endothelial quiescence, mitochondrial activity and p53 signaling are independent of the co-expressed miR-23a, miR-27a and miR-24-2.

***MIRIAL* regulates endothelial quiescence through FOXO1 and MYC signaling**

To uncover the underlying mechanism by which *MIRIAL* regulates mitochondrial biogenesis, we investigated the involvement of key transcription factors that govern endothelial metabolism and quiescence, namely FOXO1 and MYC (also known as c-myc). FOXO1 and MYC are known to exhibit antagonistic roles in the endothelium. Under conditions lacking growth factor stimulation, FOXO1 inhibits MYC signaling and promotes endothelial quiescence by decreasing proliferation and metabolism [14]. However, upon stimulation with growth factors, e.g. VEGF-A, this balance shifts towards enhanced MYC signaling. VEGF-A leads to an increase of Akt kinase activity, resulting in phosphorylation of FOXO1, subsequent nuclear export and proteasomal degradation [54].

By comparing gene sets of FOXO1 target genes (obtained from GSEA Molecular Signatures Database C3 https://www.gsea-msigdb.org/gsea/msigdb/human/geneset/FOXO1_02.html) and MYC mitochondrial target genes (obtained from [55]) to expression of all genes after *MIRIAL* knockdown, we observed a robust downregulation (left-shift) of the FOXO1 target genes, and an overall upregulation (right-shift) of mitochondrial target genes encoded in the nucleus and controlled by MYC **(Fig. 4A)**.

After *MIRIAL* knockdown, we observed an increase in *MYC* expression in RNA-sequencing **(Supp. Fig. 6A)**, qRT-PCR **(Fig. 4B)** and at protein level in Western blot **(Fig. 4C)**.

Simultaneously, *FOXO1* expression was decreased in RNA-sequencing **(Supp. Fig. 6B)**, qRT-PCR **(Fig. 4D)** and at protein level **(Fig. 4E)**. Additionally, we found elevated levels of FOXO1 phosphorylation at Ser256 **(Fig. 4F)** and an increased ratio of phospho-FOXO1/total FOXO1 **(Fig. 4G)**. Both are indicative of inactivation, nuclear export, and subsequent degradation of FOXO1. Activation of the anabolic transcription factor MYC leads to the exhaustion of energy reserves, which in turn triggers the activation of AMP-activated kinase (AMPK), a key sensor of cellular energy status [56, 57]. Under conditions of a high AMP:ATP ratio, activated AMPK can attenuate the cell cycle through p53 phosphorylation at Ser15 until energy stocks are replenished [58-60]. We assessed whether AMPK activation links MYC to the induction of the p53 signaling pathway after *MIRIAL* knockdown using Western blot analysis. Protein levels of AMPK **(Fig. 4H)** and its activated, phosphorylated (Thr172) form **(Fig. 4I)** were both increased. MYC is a potent regulator of mitochondrial biogenesis and respiration [61, 62]. So, we hypothesized that the upregulation of MYC after *MIRIAL* silencing is responsible for the induction of mitochondrial function. To test this hypothesis, we performed siRNA-mediated knockdown of MYC in conjunction with *MIRIAL* knockdown. The resulting abrogation of *MIRIAL* depletion-mediated increase in mtDNA content demonstrated that MYC is indeed essential for the regulation of mitochondrial biogenesis by *MIRIAL* **(Fig. 4J)**.

***MIRIAL* forms *RNA*·DNA:DNA triplexes in the *FOXO1* promoter region**

One mechanism by which lncRNAs can influence transcription is through direct RNA-DNA interaction. This interaction can be facilitated by bound proteins or can be protein-independent through sequence-specific *RNA*·DNA:DNA triplex formation. By the latter mechanism, lncRNAs can regulate gene expression through chromatin remodeling and recruitment of epigenetic modifiers. Examples include the lncRNAs *Sarrah* [7], *MEG3* [63] and

HIF1α-AS1 [9]. In our study, we observed that *MIRIAL* is primarily associated with the chromatin in subcellular fractionation experiments **(Fig. 3A)**. Given its localization, we investigated whether *MIRIAL* can form triplexes with double-stranded DNA. We analyzed potential triplex-forming regions (TFRs) in *MIRIAL* using *TriplexAligner* [40] and found one region within *MIRIAL* that has a high propensity for predicted triplex formation with double-stranded DNA **(Fig. 5A)**. *MIRIAL* has previously been described as containing four transposable elements that belong to the class of short, interspersed elements (SINEs), more precisely, *Alu* elements [24]. The TFR we identified corresponds to the localization of the first *Alu* element. Transposable elements, in particular *Alu* elements, have been proposed as functional domains of lncRNAs before, e.g. for the lncRNAs S*MANTIS (*formerly known as *MANTIS)* [64, 65], *ANRIL* [66] and *LEADR* [67].

Further, we were interested to identify potential triplex target sites of *MIRIAL*. Employing *TriplexAligner* [40], we predicted the triplex formation of *MIRIAL* with a selected list of promoters of genes that were regulated following *MIRIAL* knockdown **(Fig. 5B)**. The *FOXO1* promoter region emerged as the highest-scoring candidate in this preliminary, biased analysis. In a more unbiased, genome-wide approach, we identified the top 50 enhancers **(Fig. 5C)** (here denoted as regulatory elements (REMs) and annotated in EpiRegio (https://epiregio.de/) [41, 68]) that are predicted to be target sites of *MIRIAL* triplex formation. These regions were sorted based on their *TriplexAligner* scores (>50) and further stratified based on coverage with active chromatin marks (H3K27ac) in endothelial cells obtained from *ENCODE* [42]. This analysis provides a comprehensive view of the putative *MIRIAL* triplex target-ome in human endothelial cells. Interestingly, the *MIRIAL-FOXO1* interaction is in the top 0.15% of all predicted interactions with REMs and promoters combined and when stratified by H3K27ac signal **(Supp. Fig. 6C)**. In addition, the putative *MIRIAL* triplex target site in the *FOXO1* promoter region is not annotated as a transposable element **(Supp. Fig. 6D**, repeats

track). However, it (a) is distinct from transcription factor binding sites at the *FOXO1* promoter, (b) encompasses multiple REMs and (c) is an active regulatory region highly enriched in H3K27ac and H3K4me3 histone marks, which are indicative of its likely involvement in the control of *FOXO1* gene expression **(Supp. Fig. 6D)**.

To validate the functionality of *MIRIAL* as a triplex-forming RNA, we employed CRISPR/Cas9 to delete the *MIRIAL* TFR from its genomic locus. As the predicted TFR is located within a stretch of repetitive elements, guide RNAs (gRNAs) were strategically designed for the regions both upstream and downstream of the *Alu* sequence. This targeted knockout strategy resulted in the deletion of 1016 bp **(Fig. 5D)**. We confirmed the knockout in HUVECs by genomic DNA PCR **(Fig. 5E)** and qRT-PCR **(Fig. 5F)**. Our findings indicate that the excision of the transposable elements - including the predicted TFR - from the *MIRIAL* locus results in a downregulation of *FOXO1* **(Fig. 5G)** and an upregulation of *MYC* expression **(Fig. 5H)**, a change comparable to the effects observed following depletion of the full-length *MIRIAL* transcript **(Fig. 2G)**. Furthermore, removal of the TFR triggered an increase of mtDNA content in the cells **(Fig. 5I)**. Our results provide evidence that the four transposable elements within *MIRIAL* harbor a functional region, that appears to influence gene expression and mitochondrial biogenesis, potentially through a direct interaction with chromatin.

***MIRIAL* recruits Mortality Factor 4 Like 2 (MORF4L2) and TATA-binding Protein-associated Factor 2N (TAF15) to the *FOXO1* transcriptional start site**

To assess the mechanism underlying the transcriptional activation of *FOXO1* by *MIRIAL*, we used RNA pulldown followed by mass spectrometry to identify protein interaction partners of *MIRIAL*. Our findings validated the interaction of DDX5 and *MIRIAL* in endothelial cells, which had previously been described in HEK293T cells [24]. Among the enriched proteins, we

identified MORF4L2 as a potential interactor of *MIRIAL* **(Fig. 6A)**. MORF4L2 (also known as MRGX) is a component of the NuA4 histone acetyltransferase (HAT) complex [69]. This highly conserved complex contains the catalytic subunit TIP60 (KAT5) and is a recognized transcriptional regulator of *FOXO1* in HeLa cells and of the FOXO transcription factor *daf-16* in *C. elegans.* In both species, it has been linked to oxidative stress resistance and contributes to longevity in *C. elegans* [70]. Interestingly, other proteins from this HAT complex (the helicases RUVBL1 and 2, ACTB and ACTL6A/BAF53) were found in the RNA pulldown, although they were not enriched to the same level as MORF4L2.

We confirmed the interaction between MORF4L2 and *MIRIAL* by CLIP **(Fig. 6B)**. siRNA-mediated knockdown of *MORF4L2* **(Fig. 6C and Supp. Fig. 7A)** resulted in a significant upregulation of mtDNA content **(Fig. 6D)**, comparable to the previously observed effect of *MIRIAL* silencing **(Fig. 2G)**. Additionally, an upregulation of *MYC* could be observed following MORF4L2 depletion **(Fig. 6E)**, but there was no discernable downregulation of *FOXO1* expression **(Fig. 6F)**. Knockdown of *MORF4L2* was sufficient to upregulate the expression of another potential protein interactor of *MIRIAL*, TAF15 **(Fig. 6A and 6G)**. This protein is a component of the transcription initiation factor $TF_{II}D$ complex which makes up part of the RNA polymerase II pre-initiation complex [71]. Specifically, $TF_{II}D$ binds to the core promoter ensuring the proper positioning of RNA polymerase II [72]. The upregulation of *TAF15* could potentially compensate for the loss of *MORF4L2*. Of note, neither *TAF15* nor *MORF4L2* expression were changed following *MIRIAL* knockdown **(Supp. Fig. 7B and 7C)**. However, a knockdown of *TAF15* using siRNA **(Supp. Fig. 7D and 7E)** alongside *MORF4L2* knockdown was sufficient to significantly reduce *FOXO1* expression **(Fig. 6H)** to similar levels as *MIRIAL* knockdown. Moreover, mtDNA content **(Fig. 6I)** and *MYC* expression **(Fig. 6J)** were increased

after the double knockdown of *TAF15* and *MORF4L2*, confirming that both proteins are essential for the effects of *MIRIAL* on mitochondria.

To verify that *MIRIAL* recruits MORF4L2 and the NuA4 complex to the *FOXO1* transcriptional start site we performed chromatin immunoprecipitation (ChIP) using a MORF4L1/2 antibody and measured the *FOXO1* promoter sequence in the precipitate by qPCR. We found that MORF4L1/2 interact with the *FOXO1* promoter region **(Fig. 6K)**, and that this interaction was reduced after silencing of *MIRIAL* **(Fig. 6K)** showing that *MIRIAL* helps guiding the NuA4 complex to its genomic target site.

In conclusion, *MIRIAL* interacts with MORF4L2, a component of the NuA4 histone acetyltransferase complex. Through this interaction *MIRIAL* guides this HAT complex to the *FOXO1* promoter region to facilitate *FOXO1* transcription.

Mirial KO in mice decreases EF after acute myocardial infarction and regulates angiogenic sprouting _ex vivo_

Having elucidated the molecular mechanism of *MIRIAL* in HUVECs, we questioned whether *Mirial* depletion would have any *in vivo* consequences in a mouse model. To determine its involvement in angiogenesis *in vivo*, we created a *Mirial* knockout (KO) mouse line utilizing CRISPR/Cas9 **(Supp. Fig. 8A)**. We confirmed the successful deletion of *Mirial* in these mice **(Supp. Fig. 8B)**, while the expression of the adjacent miRNA cluster remained unaffected **(Supp. Fig. 8C)**. *Mirial* KO mice exhibited normal viability, fertility and showed no apparent basal defects. Interestingly, in contrast to the *in vitro* findings in HUVECs, we observed that the deletion of *Mirial* did not result in an elevation of mitochondrial content in the hearts of young or aged *Mirial* KO mice compared to their wild-type littermates **(Fig. 7A)**.

To evaluate the impact of *Mirial* KO on the restoration of myocardial capillarization and perfusion post-injury, we conducted acute myocardial infarction (AMI) surgery, followed by echocardiographic assessment of cardiac function and histological examination of the heart. Echocardiography was performed on the first day post-surgery, as well as at two- and four-weeks post-surgery **(Supp. Fig. 8D)**. Comparing the change of contractile function (ΔEF) from the first day post-surgery to the four-week endpoint revealed a significantly reduced ejection fraction in *Mirial* knockout animals **(Fig. 7B)**.

To assess the effects of *Mirial* loss on the cardiac phenotype following AMI at the cellular level, we performed immunohistochemical staining of serial sections of the heart **(Supp. Fig. 8E)**. Capillary density analysis revealed no change in number, size or perimeter **(Fig. 7C-7E)** of capillaries in the border zone of AMI heart sections. Moreover, histological examination following Sirius Red staining of collagen showed no significant alterations in infarct size or fibrosis after *Mirial* knockout **(Supp. Fig. 8F-8H)**.

Next, *ex vivo* angiogenic capacity was tested using the aortic ring assay with aortic samples from both young (3 months) and aged (18 months) **(Fig. 7F and 7G)** mice. In old animals basal sprouting was drastically reduced after *Mirial* KO. Additionally, confirming our previous observations of the *in vitro* sprouting assay, these *ex vivo* experiments show that endothelial cells from *Mirial* KO animals exhibit increased responsiveness to VEGF-A in in both age brackets.

Together, these experiments show that loss of *Mirial in vivo* has an adverse effect on cardiac outcome after AMI. Moreover, *Mirial* is an important regulator of VEGF-A-response and angiogenic sprouting *in vitro* and *ex vivo*.

Discussion

The present study reveals that the aging-induced lncRNA *MIRIAL* promotes endothelial cell proliferation and migration, while reducing mitochondrial mass, spare respiratory capacity and p53 signaling through modulation of the FOXO1-MYC antagonism, explicitly desensitizing endothelial cells against VEGF-A signaling. The results suggest that modulation of *MIRIAL* expression may be a promising strategy to counteract the aging-induced decline in endothelial angiogenic capacity.

Sprouting angiogenesis is a process in which new blood vessels are formed from pre-existing ones to supply oxygen and nutrients to growing tissues [73]. During angiogenic sprouting, metabolism is plastic and tightly intertwined with proliferative state [74, 75]. Although endothelial cells are generally thought to exhibit a glycolytic phenotype, recent research indicates that mitochondrial respiration plays a critical role in maintaining endothelial homeostasis and promoting angiogenesis [76-78]. Endothelial cells are able to upregulate mitochondrial respiration in response to reduced glycolysis allowing them to transition between metabolic pathways [75]. A metabolic shift towards increased reliance on mitochondrial respiration is essential for endothelial cells undergoing proliferation during sprouting angiogenesis. This provides the necessary energy to support the energy demands of endothelial cells as they proliferate and migrate to form new blood vessels [74, 79, 80]. Experimentally, this metabolic shift can be observed as higher mitochondrial content [81].

Mitochondrial respiration also contributes to the production of ROS, which act as signaling molecules to promote angiogenic processes such as proliferation and migration [82]. While *MIRIAL* knockdown was found to boost mitochondrial respiration and angiogenic sprouting stimulated by VEGF-A, no alteration in ROS production was observed. We propose that the

observed effect might be partially ascribed to the activation of the p53 signaling pathway, which results in the upregulation of the heme oxygenase 1 gene (*HMOX1*). HMOX1 is known to exert cytoprotective effects by reducing ROS production and enhancing the expression of proteins with antioxidant and anti-inflammatory properties [83, 84].

Additionally, mitochondrial dynamics, including fusion and fission, are involved in sprouting angiogenesis by regulating mitochondrial distribution and function within endothelial cells. In particular, OPA1 and mitochondrial complex III are crucial for angiogenesis [85, 86]. *MIRIAL* knockdown was shown to increase overall fission and fusion. Examination of the mitochondrial network morphology revealed an augmented fragmentation count, reduced branching, and unaltered average length of mitochondria. We deduce that the rise in mitochondrial mass and DNA content can be ascribed to an increased number of mitochondria exhibiting undisturbed integrity, along with enhanced dynamics and turnover, while maintaining a balanced fission and fusion equilibrium.

Endothelial metabolism is tightly interconnected with endothelial activation state, quiescence and angiogenic response. The transcription factor FOXO1 is known as the gatekeeper of endothelial quiescence. FOXO1 decreases proliferation and reduces metabolic activity of endothelial cells through repression of MYC [14]. MYC is a transcription factor that regulates the expression of many genes involved in cellular processes such as cell growth, proliferation, and metabolism [55, 87]. Research has demonstrated that MYC is capable of directly and indirectly regulating the expression of genes critical to mitochondrial biogenesis [61], including those involved in mitochondrial transcription and translation, protein import into mitochondria, and in assembly of the respiratory chain complexes [55]. In addition, to regulating metabolic and proliferative activity of endothelial cells, MYC also plays a key role in angiogenic signaling

as a downstream effector of the VEGF-A – VEGFR2 – PI3K – Akt – FOXO1 axis as well as effector of the YAP/TAZ signaling cascade [88].

Activation of MYC, and accompanying depletion of cellular ATP reservoirs, has been demonstrated to cause activation of AMPK [56, 57] and phosphorylation of p53 at serine 15, thereby leading to its stabilization and activation [59]. When *MIRIAL* is knocked down, both the AMPK and p53 signaling pathways become activated. Despite this, ATP levels do not decrease, but in fact increase. We believe that this is due to the compensatory increase in mitochondrial respiration, which leads to more efficient ATP production.

In the present study, the finding that *MIRIAL* knockdown in HUVECs and *Mirial* knockout in mice had divergent effects on angiogenic sprouting if VEGF-A was administered compared to basal conditions was of particular interest. Under unstimulated conditions loss of *MIRIAL* leads to a decrease in sprouting. This phenotype can be attributed to the accompanying induction of the p53 pathway and decreases in migration and proliferation. However, we show that VEGF-A administration not only rescues the effect of *MIRIAL* KD on proliferation, but also leads to overshooting angiogenic sprouting, both *in vitro* and *ex vivo*. We hypothesize that this is due to a strong induction of MYC through VEGFR2 signaling [89], which overrules the effects of p53 signaling.

Given our observations of angiogenic sprouting post-VEGF-A stimulation *in vitro* and *ex vivo*, it was unexpected that the capillary density measurements exhibited no differences in *Mirial* KO animals after AMI. A possible explanation for this discrepancy could be the local concentration of VEGF-A in the heart after AMI, which might be lower than in the *in vitro* and *ex vivo* model systems, and possibly not sufficient to stimulate angiogenic sprouting in KO animals to a similar extent. While there was no change in capillarization, infarct size or fibrosis

after AMI, a noticeable reduction in the change of ejection fraction was observed. This may be due to an as-yet-undefined function of *Mirial* in cardiomyocytes, which could potentially enhance or protect contractile function after AMI.

In mice, decreased expression of *Mirial* has been linked to reduced FoxO signaling, whereas an increase in *Mirial* was observed in the hippocampi of adult mice following propofol administration [20]. In our *Mirial* KO mouse model, the regulation of FoxO signaling could not be confirmed. Of particular note is the conservation level of *MIRIAL*. Whereas there is a high level of conservation of *MIRIAL* among primates [24], a comparison of the human and mouse orthologues of *MIRIAL* shows that the mouse transcript of *Mirial* is significantly shorter compared to the human orthologue (690 bp versus 1774 bp) and lacks the *Alu* element-containing domains, as *Alu* elements are only conserved in primates [90, 91]. We conclude that human *MIRIAL* and mouse *Mirial* are only partially functionally conserved, and that human *MIRIAL* alters gene expression *via* a triplex-dependent mechanism that is not evident in mice.

The results of the present study show that *MIRIAL* is a quiescence-promoting lncRNA that induces *FOXO1* expression through triplex formation in the *FOXO1* promoter region. Numerous proteins that potentially interact with *MIRIAL* or that are regulated by *MIRIAL* have been examined in order to elucidate the mechanism by which *MIRIAL* regulates endothelial cell function. Proteins that we proved not to be accountable for the MYC-mediated increase in mtDNA content include the prohibitins PHB and PHB2, p53, AMP-activated protein kinase (AMPK), DEAD box Protein 5 (DDX5), mitochondrial ribosomal protein L 41 (MRPL41), protein activator of interferon induced protein kinase (PRKRA), mitochondrial serine/threonine-protein phosphatase (PGAM5), peroxisome proliferator-activated receptor gamma coactivator 1-beta (PGC1β), purine-rich element binding protein A and B (PURA and PURB),

NF-κB p65 subunit (RELA), RNA-binding protein Fused in Sarcoma (FUS) and the far upstream element-binding protein 3 (FUBP3) (data not shown). The interaction between DDX5 and *MIRIAL* has been described before in HEK293T cells [24]. In the present study, we demonstrate that DDX5 as well as MRPL41 are essential for the upregulation of p53 target genes, but not for the increase of mtDNA content after *MIRIAL* knockdown.

RNA·DNA:DNA triple helix formation as a mechanism of gene expression regulation has been previously described for several other lncRNAs. These include *Sarrah*, which is decreased during aging and has anti-apoptotic properties in HL-1 cardiomyocytes [7] and *HIF1α-AS1* which through triplex formation recruits the HUSH complex resulting in the repression of target genes such as EPH receptor A and Adrenomedullin in endothelial cells [92].

The putative triplex-forming region of *MIRIAL*, that is predicted to interact with the *FOXO1* promoter region, contains an *Alu* element. Interestingly, lncRNAs, like S*MANTIS* [64] and *ANRIL* [66], have been described to contain *Alu* elements as functional regions. In various endothelial cell types, the *Alu* element of the lncRNA S*MANTIS* restricts the expression of ICAM-1, hence decreasing monocyte adhesion, which plays a critical role in the pathogenesis of atherosclerosis in humans [65]. *ANRIL* is currently recognized as one of the most potent genetic contributors to atherosclerosis, and its expression level is linked to the severity of the disease. Mechanistically, *ANRIL* may serve as a framework for directing effector proteins to chromatin, a process that relies on the presence of an *Alu* motif that can be found within the *ANRIL* transcript and is repeated thousands of times throughout the genome as well as in *ANRIL* target gene promoters, contributing to the effectiveness of this interaction [66]. On the other hand, the lncRNA *KCNQ1OT1* contains a transposable element of the L1 class capable of forming a triplex with L1 and *Alu* elements on genomic DNA [93]. However, unlike the

aforementioned examples, our study is the first to describe a triplex-forming *Alu* element within a lncRNA. This unique feature sets *MIRIAL* apart from other lncRNAs that have been studied until now.

Conclusion

Taken together, *MIRIAL* is an aging-induced lncRNA which acts as a key regulator of endothelial metabolic and cellular function. *MIRIAL* promotes cell proliferation, migration and basal angiogenic sprouting while decreasing mitochondrial function. However, silencing *MIRIAL* in pro-angiogenic conditions improves angiogenesis. We hypothesize that *MIRIAL* influences these cellular functions by affecting the p53 pathway and mitochondrial respiration through FOXO1 signaling. These results suggest that transcriptional modulation of *MIRIAL*, particularly in the elderly, might be a good strategy to improve therapeutic angiogenesis.

Novelty and significance

What is known?

- Aging induces endothelial dysfunction
- lncRNAs regulate cellular functions
- *MIRIAL* is a lncRNA

What new information does this article contribute?

- *MIRIAL* is upregulated by aging in endothelial cells
- *MIRIAL* controls mitochondrial function in endothelial cells
- *MIRIAL* regulates endothelial metabolism through modulation of FOXO1 and MYC
- *MIRIAL* regulates cell cycle progression through suppression of p53 signaling

Summary

This study represents the first comprehensive characterization of the lncRNA *MIRIAL*, offering mechanistic insight into its mode of action in endothelial cells. *MIRIAL* is the first-described lncRNA containing an *Alu* element which can form an *RNA*·DNA:DNA triple helix with genomic DNA. *MIRIAL* regulates the expression of the quiescence promoting *FOXO1* by forming a triplex within the *FOXO1* promoter region. The expression of *FOXO1*, in turn, suppresses MYC signaling and mitochondrial biogenesis and metabolism. By repressing p53 signaling, *MIRIAL* facilitates cell cycle progression, migration and basal angiogenic sprouting. In mice, loss of *Mirial* leads to a reduction of myocardial contractile function following acute myocardial infarction. In addition, *Mirial* knockout leads to increased responsiveness of endothelial cells towards VEGF-A stimulation in *ex vivo* settings.

Acknowledgments and sources of funding

This work was supported by the Goethe University Frankfurt/Main, Germany, the Deutsche Forschungsgemeinschaft (DFG) excellence cluster EXS2026 (Cardio-Pulmonary Institute, Project number 390649896), the DFG Transregio project TRR267 (project number 403584255, project B04 (to RAB and LM), B03 and A01 (to SD), A04 (to MSL), A06 (to RPB), and Z02 (to IK)), the DFG collaborative research centre SFB 834 (project B09), the German Centre for Cardiovascular Research (DZHK), an European Research Council (ERC) starting grant (NOVA), and an ERC consolidator grant (NICCA). The graphical abstract was created with BioRender.com.

Author contributions

CK, KT, and RAB conceptualized and designed the study. CK, SK, TW, KT, AF, RPJ, MMR, DB, FL, FV, JUGW, JS, ATG, LS, SG, IW, LM and MSL acquired, analyzed, and interpreted data. CK drafted the manuscript. All authors critically revised the manuscript and approved the final version to be published.

Disclosures/Conflicts of interest

The authors have nothing to declare.

List of Supplemental Materials:

1. Supplemental figures and legends 1-8
2. Major Resources Table

References

1. Boon RA, Jaé N, Holdt L, Dimmeler S. Long noncoding rnas: From clinical genetics to therapeutic targets? *Journal of the American College of Cardiology*. 2016;67:1214-1226
2. Quinn JJ, Chang HY. Unique features of long non-coding rna biogenesis and function. *Nature Reviews Genetics*. 2016;17:47-62
3. Bhat SA, Ahmad SM, Mumtaz PT, Malik AA, Dar MA, Urwat U, et al. Long non-coding rnas: Mechanism of action and functional utility. *Non-coding RNA Research*. 2016;1:43-50
4. Hoogsteen K. The structure of crystals containing a hydrogen-bonded complex of 1-methylthymine and 9-methyladenine. *Acta crystallographica*. 1959;12:822-823
5. Rajagopal P, Feigon J. Triple-strand formation in the homopurine:Homopyrimidine DNA oligonucleotides d(g-a)4 and d(t-c)4. *Nature*. 1989;339:637-640
6. Felsenfeld G, Davies DR, Rich A. Formation of a three-stranded polynucleotide molecule. *Journal of the American Chemical Society*. 1957;79:2023-2024
7. Trembinski DJ, Bink DI, Theodorou K, Sommer J, Fischer A, van Bergen A, et al. Aging-regulated anti-apoptotic long non-coding rna sarrah augments recovery from acute myocardial infarction. *Nature communications*. 2020;11:2039
8. Kalwa M, Hänzelmann S, Otto S, Kuo C-C, Franzen J, Joussen S, et al. The lncrna hotair impacts on mesenchymal stem cells via triple helix formation. *Nucleic Acids Research*. 2016;44:10631-10643
9. Leisegang MS, Bains JK, Seredinski S, Oo JA, Krause NM, Kuo C-C, et al. Hif1α-as1 is a DNA:DNA:Rna triplex-forming lncrna interacting with the hush complex. *Nature communications*. 2022;13:6563
10. Mc Namara K, Alzubaidi H, Jackson JK. Cardiovascular disease as a leading cause of death: How are pharmacists getting involved? *Integrated pharmacy research & practice*. 2019;8:1-11
11. Niccoli T, Partridge L. Ageing as a risk factor for disease. *Current Biology*. 2012;22:R741-R752

12. Lakatta EG, Levy D. Arterial and cardiac aging: Major shareholders in cardiovascular disease enterprises: Part i: Aging arteries: A "set up" for vascular disease. *Circulation*. 2003;107:139-146

13. Moriya J, Minamino T. Angiogenesis, cancer, and vascular aging. *Front Cardiovasc Med*. 2017;4

14. Wilhelm K, Happel K, Eelen G, Schoors S, Oellerich MF, Lim R, et al. Foxo1 couples metabolic activity and growth state in the vascular endothelium. *Nature*. 2016;529:216-220

15. Martins R, Lithgow GJ, Link W. Long live foxo: Unraveling the role of foxo proteins in aging and longevity. *Aging cell*. 2016;15:196-207

16. Morris BJ, Willcox DC, Donlon TA, Willcox BJ. Foxo3: A major gene for human longevity - a mini-review. *Gerontology*. 2015;61:515-525

17. Paik J-H, Kollipara R, Chu G, Ji H, Xiao Y, Ding Z, et al. Foxos are lineage-restricted redundant tumor suppressors and regulate endothelial cell homeostasis. *Cell*. 2007;128:309-323

18. Dharaneeswaran H, Abid MR, Yuan L, Dupuis D, Beeler D, Spokes KC, et al. Foxo1-mediated activation of akt plays a critical role in vascular homeostasis. *Circulation research*. 2014;115:238-251

19. Sengupta A, Chakraborty S, Paik J, Yutzey KE, Evans-Anderson HJ. Foxo1 is required in endothelial but not myocardial cell lineages during cardiovascular development. *Developmental dynamics : an official publication of the American Association of Anatomists*. 2012;241:803-813

20. Fan J, Zhou Q, Li Y, Song X, Hu J, Qin Z, et al. Profiling of long non-coding rnas and mrnas by rna-sequencing in the hippocampi of adult mice following propofol sedation. *Frontiers in molecular neuroscience*. 2018;11:91

21. Fan C, Tang Y, Wang J, Wang Y, Xiong F, Zhang S, et al. Long non-coding rna loc284454 promotes migration and invasion of nasopharyngeal carcinoma via modulating the rho/rac signaling pathway. *Carcinogenesis*. 2019;40:380-391

22. Han L, Zhou W, Wu F. Long non-coding rna loc284454 promotes hepatocellular carcinoma cell invasion and migration by inhibiting e-cadherin expression. *Oncology reports*. 2021;45

23. Liu H, Gu X, Wang G, Huang Y, Ju S, Huang J, et al. Copy number variations primed lncrnas deregulation contribute to poor prognosis in colorectal cancer. *Aging*. 2019;11:6089-6108

24. Das M, Renganathan A, Dighe SN, Bhaduri U, Shettar A, Mukherjee G, et al. Ddx5/p68 associated lncrna loc284454 is differentially expressed in human cancers and modulates gene expression. *RNA biology*. 2018;15:214-230

25. Fan C, Wang J, Tang Y, Zhang S, Xiong F, Guo C, et al. Upregulation of long non-coding rna loc284454 may serve as a new serum diagnostic biomarker for head and neck cancers. *BMC cancer*. 2020;20:917

26. Bonauer A, Carmona G, Iwasaki M, Mione M, Koyanagi M, Fischer A, et al. Microrna-92a controls angiogenesis and functional recovery of ischemic tissues in mice. *Science*. 2009;324:1710-1713

27. Baker M, Robinson SD, Lechertier T, Barber PR, Tavora B, D'Amico G, et al. Use of the mouse aortic ring assay to study angiogenesis. *Nature protocols*. 2011;7:89-104

28. Concordet J-P, Haeussler M. Crispor: Intuitive guide selection for crispr/cas9 genome editing experiments and screens. *Nucleic Acids Research*. 2018;46:W242-W245

29. Sanjana NE, Shalem O, Zhang F. Improved vectors and genome-wide libraries for crispr screening. *Nature methods*. 2014;11:783-784

30. Gimbel AT, Koziarek S, Theodorou K, Schulz JF, Stanicek L, Ali T, et al. Aging-regulated tug1 is dispensable for endothelial cell function. *PLoS One*. 2022:2022.2002.2027.482212

31. Cawthon RM. Telomere measurement by quantitative pcr. *Nucleic Acids Res*. 2002;30:e47

32. Takagawa J, Zhang Y, Wong ML, Sievers RE, Kapasi NK, Wang Y, et al. Myocardial infarct size measurement in the mouse chronic infarction model: Comparison of area- and length-based approaches. *Journal of applied physiology (Bethesda, Md. : 1985)*. 2007;102:2104-2111

33. Aslan GS, Jaé N, Manavski Y, Fouani Y, Shumliakivska M, Kettenhausen L, et al. Malat1 deficiency prevents neonatal heart regeneration by inducing cardiomyocyte binucleation. *JCI insight*. 2023;8

34. Huang da W, Sherman BT, Lempicki RA. Systematic and integrative analysis of large gene lists using david bioinformatics resources. *Nature protocols*. 2009;4:44-57

35. Sherman BT, Hao M, Qiu J, Jiao X, Baseler MW, Lane HC, et al. David: A web server for functional enrichment analysis and functional annotation of gene lists (2021 update). *Nucleic Acids Res*. 2022;50:W216-w221

36. Koopman WJ, Verkaart S, Visch HJ, van der Westhuizen FH, Murphy MP, van den Heuvel LW, et al. Inhibition of complex i of the electron transport chain causes o2-. -mediated mitochondrial outgrowth. *American journal of physiology. Cell physiology*. 2005;288:C1440-1450

37. Rehman J, Zhang HJ, Toth PT, Zhang Y, Marsboom G, Hong Z, et al. Inhibition of mitochondrial fission prevents cell cycle progression in lung cancer. *FASEB journal : official publication of the Federation of American Societies for Experimental Biology*. 2012;26:2175-2186

38. Durand MJ, Ait-Aissa K, Levchenko V, Staruschenko A, Gutterman DD, Beyer AM. Visualization and quantification of mitochondrial structure in the endothelium of intact arteries. *Cardiovascular research*. 2019;115:1546-1556

39. Juni RP, Al-Shama R, Kuster DWD, van der Velden J, Hamer HM, Vervloet MG, et al. Empagliflozin restores chronic kidney disease-induced impairment of endothelial regulation of cardiomyocyte relaxation and contraction. *Kidney international*. 2021;99:1088-1101

40. Warwick T, Seredinski S, Krause NM, Bains JK, Althaus L, Oo JA, et al. A universal model of rna.DNA:DNA triplex formation accurately predicts genome-wide rna-DNA interactions. *Briefings in bioinformatics*. 2022;23

41. Baumgarten N, Hecker D, Karunanithi S, Schmidt F, List M, Schulz MH. Epiregio: Analysis and retrieval of regulatory elements linked to genes. *Nucleic Acids Research*. 2020;48:W193-W199

42. Davis CA, Hitz BC, Sloan CA, Chan ET, Davidson JM, Gabdank I, et al. The encyclopedia of DNA elements (encode): Data portal update. *Nucleic Acids Research*. 2017;46:D794-D801

43. Fasolo F, Winski G, Li Z, Wu Z, Winter H, Ritzer J, et al. The circular rna ataxia telangiectasia mutated regulates oxidative stress in smooth muscle cells in expanding abdominal aortic aneurysms. *Molecular therapy. Nucleic acids*. 2023;33:848-865

44. Wagner JUG, Tombor LS, Malacarne PF, Kettenhausen L-M, Panthel J, Kujundzic H, et al. Aging impairs the neurovascular interface in the heart. *Science*. 2023;381:897-906

45. Pearson WR, Lipman DJ. Improved tools for biological sequence comparison. *Proceedings of the National Academy of Sciences of the United States of America*. 1988;85:2444-2448

46. Drekolia MK, Talyan S, Cordellini Emídio R, Boon RA, Guenther S, Looso M, et al. Unravelling the impact of aging on the human endothelial lncrna transcriptome. *Frontiers in genetics*. 2022;13:1035380

47. Huang X, Miller W. A time-efficient, linear-space local similarity algorithm. *Advances in Applied Mathematics*. 1991;12:337-357

48. Wang L, Park HJ, Dasari S, Wang S, Kocher JP, Li W. Cpat: Coding-potential assessment tool using an alignment-free logistic regression model. *Nucleic Acids Res*. 2013;41:e74

49. Krützfeldt A, Spahr R, Mertens S, Siegmund B, Piper HM. Metabolism of exogenous substrates by coronary endothelial cells in culture. *Journal of Molecular and Cellular Cardiology*. 1990;22:1393-1404

50. De Bock K, Georgiadou M, Schoors S, Kuchnio A, Wong Brian W, Cantelmo Anna R, et al. Role of pfkfb3-driven glycolysis in vessel sprouting. *Cell*. 2013;154:651-663

51. Youle RJ, van der Bliek AM. Mitochondrial fission, fusion, and stress. *Science*. 2012;337:1062-1065

52. Colman MS, Afshari CA, Barrett JC. Regulation of p53 stability and activity in response to genotoxic stress. *Mutation Research/Reviews in Mutation Research*. 2000;462:179-188

53. Fiedler J, Jazbutyte V, Kirchmaier BC, Gupta SK, Lorenzen J, Hartmann D, et al. Microrna-24 regulates vascularity after myocardial infarction. *Circulation*. 2011;124:720-730

54. Greer EL, Brunet A. Foxo transcription factors at the interface between longevity and tumor suppression. *Oncogene*. 2005;24:7410-7425

55. Morrish F, Hockenbery D. Myc and mitochondrial biogenesis. *Cold Spring Harbor perspectives in medicine*. 2014;4

56. Liu L, Ulbrich J, Müller J, Wüstefeld T, Aeberhard L, Kress TR, et al. Deregulated myc expression induces dependence upon ampk-related kinase 5. *Nature*. 2012;483:608-612

57. Nieminen AI, Eskelinen VM, Haikala HM, Tervonen TA, Yan Y, Partanen JI, et al. Myc-induced ampk-phospho p53 pathway activates bak to sensitize mitochondrial apoptosis. *Proceedings of the National Academy of Sciences of the United States of America*. 2013;110:E1839-1848

58. Jones RG, Plas DR, Kubek S, Buzzai M, Mu J, Xu Y, et al. Amp-activated protein kinase induces a p53-dependent metabolic checkpoint. *Molecular cell*. 2005;18:283-293

59. Kruse JP, Gu W. Snapshot: P53 posttranslational modifications. *Cell*. 2008;133:930-930.e931

60. Haikala HM, Anttila JM, Klefström J. Myc and ampk-save energy or die! *Frontiers in cell and developmental biology*. 2017;5:38

61. Li F, Wang Y, Zeller KI, Potter JJ, Wonsey DR, O'Donnell KA, et al. Myc stimulates nuclearly encoded mitochondrial genes and mitochondrial biogenesis. *Molecular and cellular biology*. 2005;25:6225-6234

62. Goetzman ES, Prochownik EV. The role for myc in coordinating glycolysis, oxidative phosphorylation, glutaminolysis, and fatty acid metabolism in normal and neoplastic tissues. *Front Endocrinol (Lausanne).* 2018;9

63. Mondal T, Subhash S, Vaid R, Enroth S, Uday S, Reinius B, et al. Meg3 long noncoding rna regulates the tgf-β pathway genes through formation of rna-DNA triplex structures. *Nature communications*. 2015;6:7743

64. Leisegang MS, Fork C, Josipovic I, Richter FM, Preussner J, Hu J, et al. Long noncoding rna mantis facilitates endothelial angiogenic function. *Circulation*. 2017;136:65-79

65. Leisegang MS, Bibli S-I, Günther S, Pflüger-Müller B, Oo JA, Höper C, et al. Pleiotropic effects of laminar flow and statins depend on the krüppel-like factor-induced lncrna mantis. *European Heart Journal*. 2019;40:2523-2533

66. Holdt LM, Hoffmann S, Sass K, Langenberger D, Scholz M, Krohn K, et al. Alu elements in anril non-coding rna at chromosome 9p21 modulate atherogenic cell functions through trans-regulation of gene networks. *PLoS genetics*. 2013;9:e1003588

67. Bezzecchi E, Pagani G, Forte B, Percio S, Zaffaroni N, Dolfini D, et al. Mir205hg/leadr long noncoding rna binds to primed proximal regulatory regions in prostate basal cells through a triplex- and alu-mediated mechanism. *Frontiers in cell and developmental biology*. 2022;10

68. Schmidt F, Marx A, Baumgarten N, Hebel M, Wegner M, Kaulich M, et al. Integrative analysis of epigenetics data identifies gene-specific regulatory elements. *Nucleic Acids Research*. 2021;49:10397-10418

69. Devoucoux M, Roques C, Lachance C, Lashgari A, Joly-Beauparlant C, Jacquet K, et al. Mrg proteins are shared by multiple protein complexes with distinct functions. *Molecular & Cellular Proteomics*. 2022;21:100253

70. Ikeda T, Uno M, Honjoh S, Nishida E. The myst family histone acetyltransferase complex regulates stress resistance and longevity through transcriptional control of daf-16/foxo transcription factors. *EMBO reports*. 2017;18:1716-1726

71. Bertolotti A, Lutz Y, Heard DJ, Chambon P, Tora L. Htaf(ii)68, a novel rna/ssdna-binding protein with homology to the pro-oncoproteins tls/fus and ews is associated with both tfiid and rna polymerase ii. *The EMBO journal*. 1996;15:5022-5031

72. Louder RK, He Y, López-Blanco JR, Fang J, Chacón P, Nogales E. Structure of promoter-bound tfiid and model of human pre-initiation complex assembly. *Nature*. 2016;531:604-609

73. Eelen G, Treps L, Li X, Carmeliet P. Basic and therapeutic aspects of angiogenesis updated. *Circulation research*. 2020;127:310-329

74. Yetkin-Arik B, Vogels IMC, Neyazi N, van Duinen V, Houtkooper RH, van Noorden CJF, et al. Endothelial tip cells in vitro are less glycolytic and have a more flexible response to metabolic stress than non-tip cells. *Scientific reports*. 2019;9:10414

75. Yetkin-Arik B, Vogels IMC, Nowak-Sliwinska P, Weiss A, Houtkooper RH, Van Noorden CJF, et al. The role of glycolysis and mitochondrial respiration in the formation and functioning of endothelial tip cells during angiogenesis. *Scientific reports*. 2019;9:12608

76. Davidson SM, Duchen MR. Endothelial mitochondria: Contributing to vascular function and disease. *Circulation research*. 2007;100:1128-1141

77. Dranka BP, Hill BG, Darley-Usmar VM. Mitochondrial reserve capacity in endothelial cells: The impact of nitric oxide and reactive oxygen species. *Free Radical Biology and Medicine*. 2010;48:905-914

78. Schleicher M, Shepherd BR, Suarez Y, Fernandez-Hernando C, Yu J, Pan Y, et al. Prohibitin-1 maintains the angiogenic capacity of endothelial cells by regulating mitochondrial function and senescence. *Journal of Cell Biology*. 2008;180:101-112

79. Al-Mehdi A-B, Pastukh VM, Swiger BM, Reed DJ, Patel MR, Bardwell GC, et al. Perinuclear mitochondrial clustering creates an oxidant-rich nuclear domain required for hypoxia-induced transcription. *Sci Signal*. 2012;5:ra47-ra47

80. Coutelle O, Hornig-Do H-T, Witt A, Andree M, Schiffmann LM, Piekarek M, et al. Embelin inhibits endothelial mitochondrial respiration and impairs neoangiogenesis during tumor growth and wound healing. *EMBO Mol Med*. 2014;6:624-639

81. Wright GL, Maroulakou IG, Eldridge J, Liby TL, Sridharan V, Tsichlis PN, et al. Vegf stimulation of mitochondrial biogenesis: Requirement of akt3 kinase. *FASEB journal : official publication of the Federation of American Societies for Experimental Biology*. 2008;22:3264-3275

82. Takac I, Schröder K, Brandes RP. The nox family of nadph oxidases: Friend or foe of the vascular system? *Current Hypertension Reports*. 2012;14:70-78

83. Chiang SK, Chen SE, Chang LC. The role of ho-1 and its crosstalk with oxidative stress in cancer cell survival. *Cells*. 2021;10

84. Seiwert N, Wecklein S, Demuth P, Hasselwander S, Kemper TA, Schwerdtle T, et al. Heme oxygenase 1 protects human colonocytes against ros formation, oxidative DNA damage and cytotoxicity induced by heme iron, but not inorganic iron. *Cell Death & Disease*. 2020;11:787

85. Diebold LP, Gil HJ, Gao P, Martinez CA, Weinberg SE, Chandel NS. Mitochondrial complex iii is necessary for endothelial cell proliferation during angiogenesis. *Nature metabolism*. 2019;1:158-171

86. Schuler M-H, Hughes AL. Opa1 and angiogenesis: Beyond the fusion function. *Cell Metabolism*. 2020;31:886-887

87. Das SK, Lewis BA, Levens D. Myc: A complex problem. *Trends in Cell Biology*. 2023;33:235-246

88. Hofmann M, Heineke J. The impact of endothelial transcription factors in sprouting angiogenesis. In: Marmé D, ed. *Tumor angiogenesis: A key target for cancer therapy*. Cham: Springer International Publishing; 2018:1-18.

89. Dang Chi V. Myc on the path to cancer. *Cell*. 2012;149:22-35

90. Arcot SS, Wang Z, Weber JL, Deininger PL, Batzer MA. Alu repeats: A source for the genesis of primate microsatellites. *Genomics*. 1995;29:136-144

91. Deininger P. Alu elements: Know the sines. *Genome Biology*. 2011;12:236

92. Leisegang MS, Bains JK, Seredinski S, Oo JA, Krause NM, Kuo CC, et al. Hif1α-as1 is a DNA:DNA:Rna triplex-forming lncrna interacting with the hush complex. *Nature communications*. 2022;13:6563

93. Zhang X, Jiang Q, Li J, Zhang S, Cao Y, Xia X, et al. Kcnq1ot1 promotes genome-wide transposon repression by guiding rna–DNA triplexes and hp1 binding. *Nature Cell Biology*. 2022;24:1617-1629

Figures

Graphical abstract

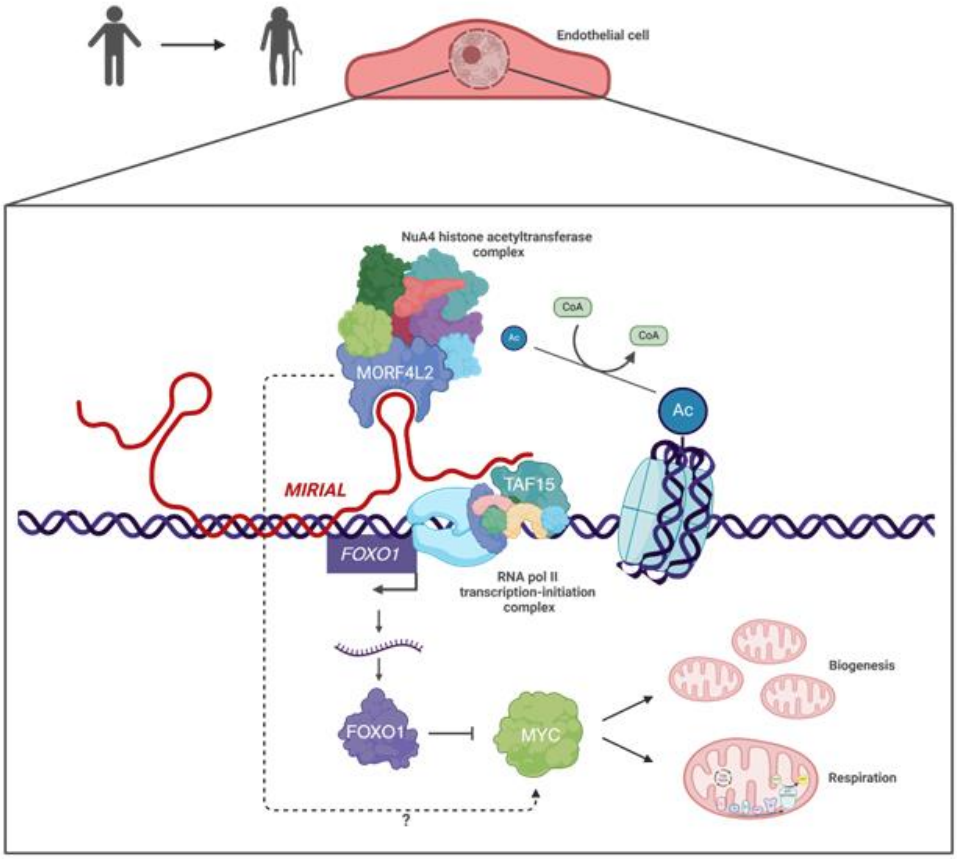

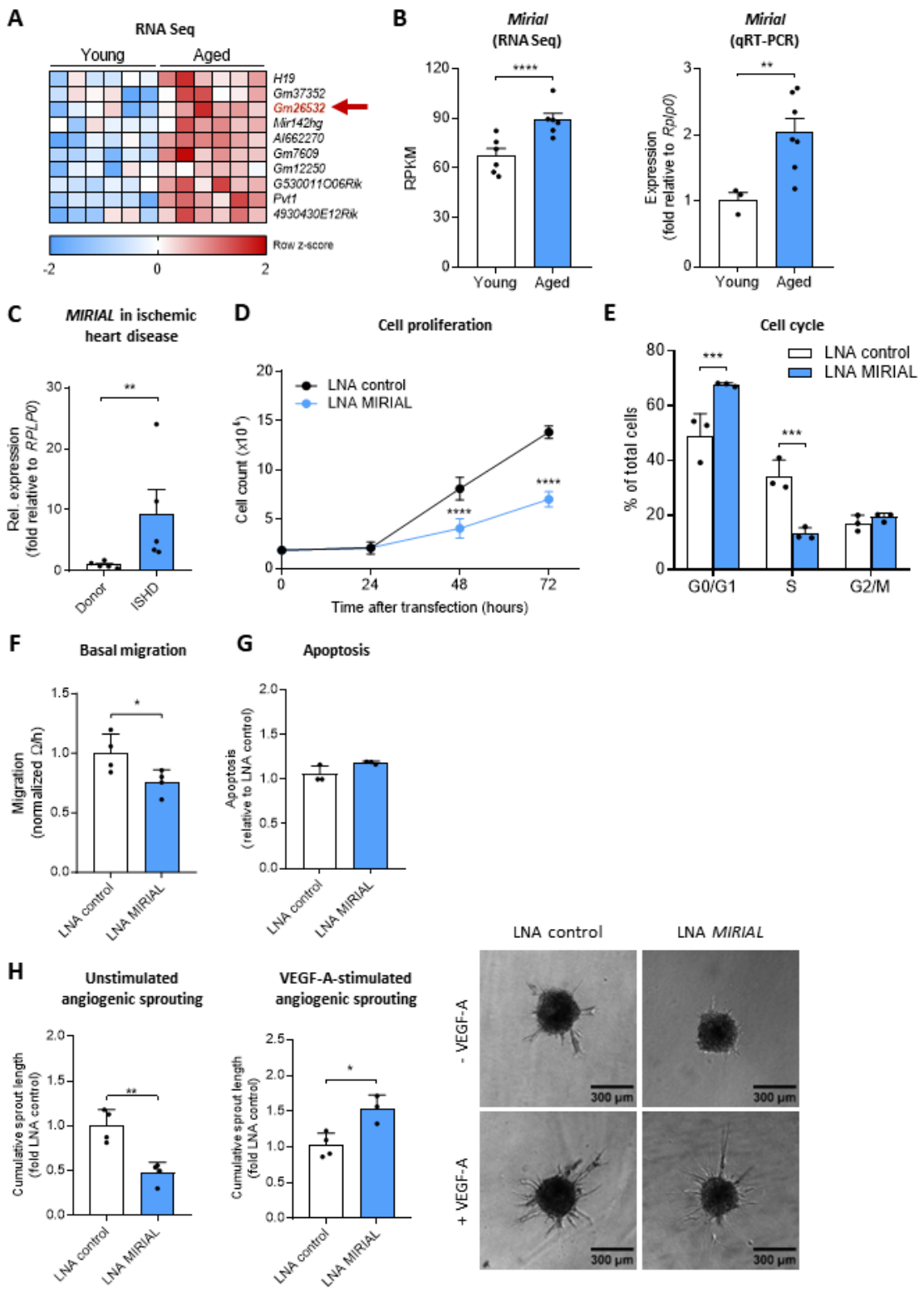

Fig. 1: *MIRIAL* is an aging-induced long non-coding RNA that regulates endothelial cell quiescence

A Heatmap representing the most significant differentially regulated lncRNAs from RNA sequencing data of cardiac ECs isolated from young (12 weeks) and aged (20 months) mice (*n*=6). **B** *Mirial* expression from RNA seq data (*n*=6; Mann-Whitney test with FDR correction) quantified from fig. 1 A and *Mirial* expression from aortic intima of young (12 weeks) and aged mice (20 months) measured by qRT-PCR (n=3 and 7; Welch's *t* test). Results are expressed as mean ± s.e.m. **C** *MIRIAL* expression in ischemic heart disease cardiac biopsies compared to healthy controls measured by qRT-PCR (*n*=5; Mann-Whitney test). Results are expressed as mean ± s.e.m. **D** Growth curve depicting the cell number of HUVECs after the indicated hours (0-72h) of gapmeR-mediated *MIRIAL* knockdown (20 nM) compared to control-transfected HUVECs (representative graph of *n*=3; ANOVA). **E** EdU combined with FxCycle flow cytometry-based cell cycle analysis of HUVECs 48h after gapmeR-mediated *MIRIAL* knockdown (20 nM) compared to control-transfected HUVECs (*n*=3; ANOVA). **F** Electric cell-substrate impedance sensing (ECIS)-based migration assay of HUVECs 48h after gapmeR-mediated *MIRIAL* knockdown (20 nM) compared to control-transfected HUVECs (*n*=4; unpaired *t* test). **G** Caspase 3/7 activity-based apoptosis assay of HUVECs 48h after gapmeR-mediated *MIRIAL* knockdown (20 nM) compared to control-transfected HUVECs (*n*=3; unpaired *t* test). **H** Cumulative sprout length in an angiogenic spheroid sprouting assay under basal and VEGF-stimulated (50 ng/mL) conditions using HUVECs 72h after gapmeR-mediated *MIRIAL* knockdown (20 nM) compared to control-transfected HUVECs (*n*=4; unpaired *t* test). 8-15 spheroids per condition were analyzed. Results are expressed as mean ± s.d. unless otherwise stated; *$p<0.05$, **$p<0.01$, ***$p<0.001$, **** $p<0.0001$

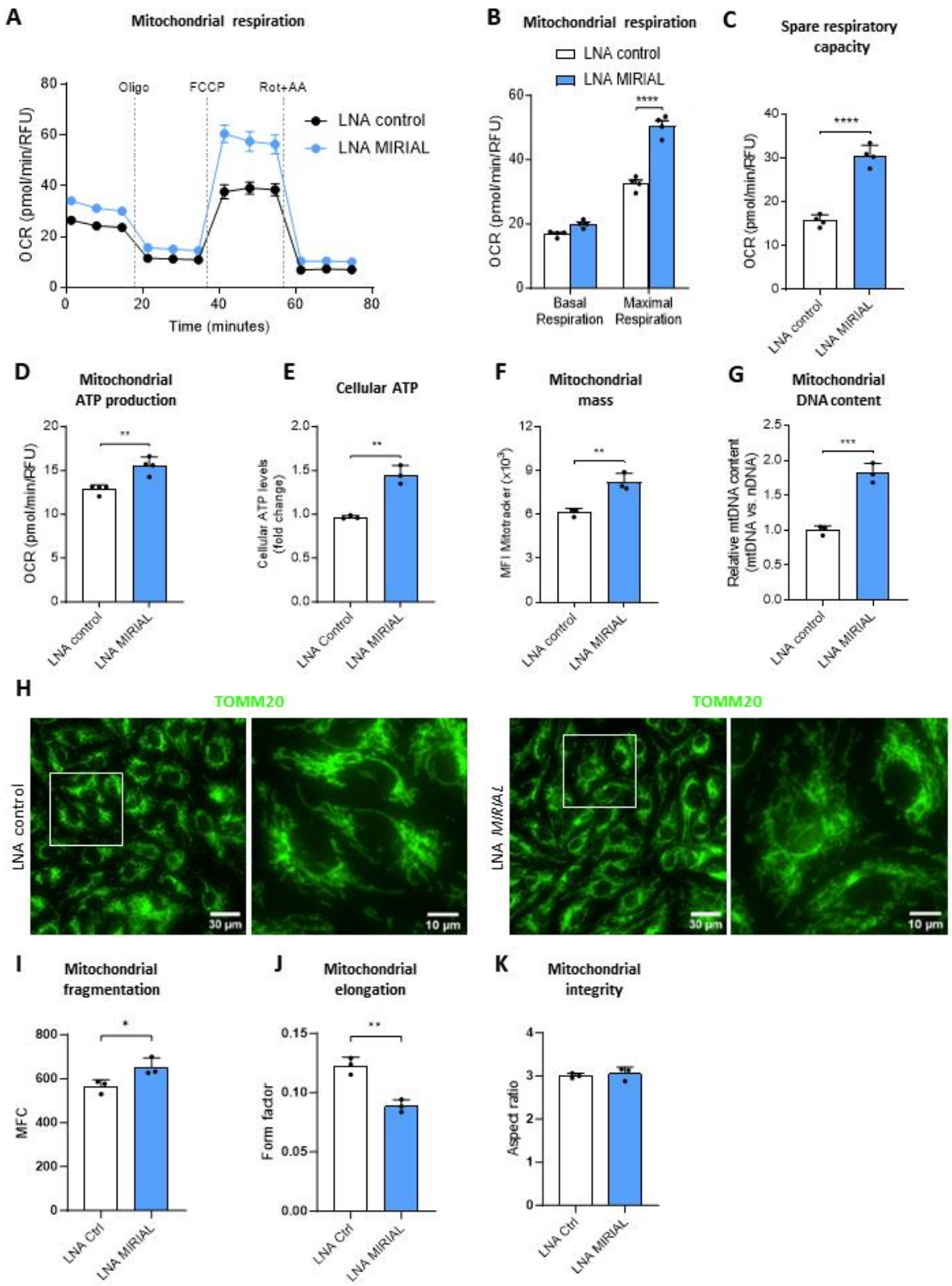

Fig. 2: *MIRIAL* regulates endothelial mitochondrial metabolism

A Oxygen consumption rate (OCR) as a measure of mitochondrial respiration in HUVECs 48h after gapmeR-mediated *MIRIAL* knockdown (20 nM) compared to control-transfected HUVECs

using Seahorse mitochondrial stress test (representative graph of *n*=4). **B** Oxygen consumption rate (OCR) as a measure of mitochondrial basal and maximal respiration in HUVECs 48h after gapmeR-mediated *MIRIAL* knockdown (20 nM) compared to control-transfected HUVECs, quantified from fig. 2 A using Seahorse mitochondrial stress test (*n*=4; ANOVA). **C** Spare respiratory capacity (SRC) of HUVECs 48h after gapmeR-mediated *MIRIAL* knockdown (20 nM) compared to control-transfected HUVECs, quantification from fig. 4A (*n*=4; unpaired *t* test). **D** Mitochondrial ATP production of HUVECs 48h after gapmeR-mediated *MIRIAL* knockdown (20 nM) compared to control-transfected HUVECs using Seahorse mitochondrial stress test (*n*=4; unpaired *t* test). **E** Cellular ATP levels of HUVECs 48h after gapmeR-mediated *MIRIAL* knockdown (20 nM) compared to control-transfected HUVECs using bioluminescence-based assay (*n*=3). **F** Mitochondrial mass of HUVECs 48h after gapmeR-mediated *MIRIAL* knockdown (20 nM) compared to control-transfected HUVECs measured by Mitotracker flow cytometry (*n*=3; unpaired *t* test). **G** Mitochondrial DNA (mtDNA) content relative to nuclear DNA (nDNA) content of HUVECs 48h after gapmeR-mediated *MIRIAL* knockdown (20 nM) compared to control-transfected HUVECs using qPCR (*n*=3; unpaired *t* test). **H** Representative images of HUVECs 48h after gapmeR-mediated *MIRIAL* knockdown (20 nM) compared to control-transfected HUVECs stained with an TOMM20 antibody and analyzed by immunofluorescence microscopy. **I** Mitochondrial fragmentation count (MFC) in HUVECs 48h after gapmeR-mediated *MIRIAL* knockdown (20 nM) compared to control-transfected HUVECs stained with an TOMM20 antibody and analyzed by immunofluorescence microscopy (*n*=3; unpaired *t* test). **J** Mitochondrial elongation measured as mitochondrial form factor in HUVECs 48h after gapmeR-mediated *MIRIAL* knockdown (20 nM) compared to control-transfected HUVECs stained with an TOMM20 antibody and analyzed by immunofluorescence microscopy (*n*=3; unpaired *t* test). **K** Mitochondrial integrity in HUVECs 48h after gapmeR-mediated *MIRIAL*

knockdown (20 nM) compared to control-transfected HUVECs stained with an TOMM20 antibody and analyzed by immunofluorescence microscopy (n=3; unpaired t test). Results are expressed as mean ± s.d.; *p<0.05, **p<0.01, ***p<0.001, **** p<0.0001

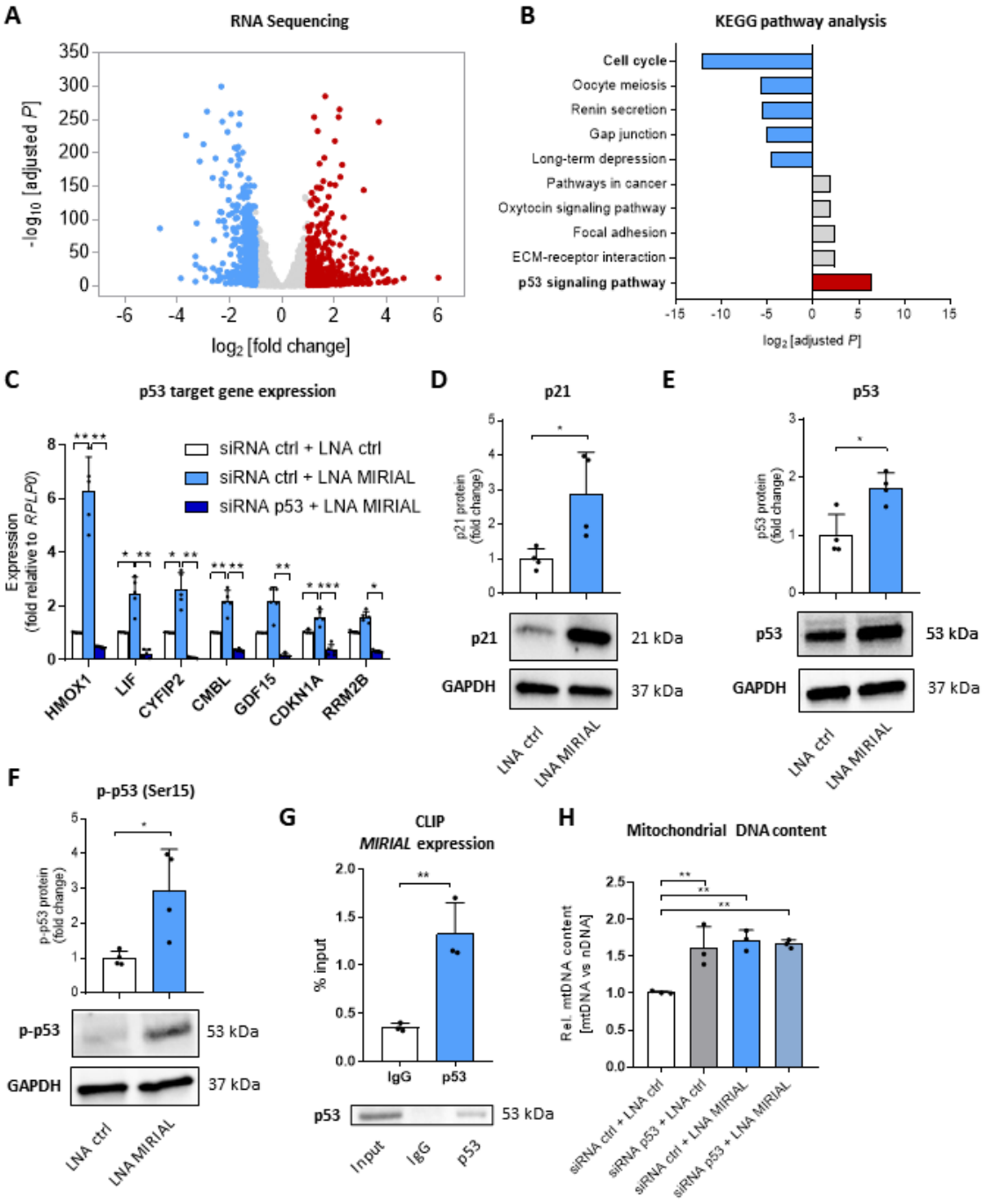

Fig. 3: *MIRIAL* knockdown in HUVECs activates the p53 signaling pathway

A Volcano plot representing differentially expressed genes from RNA sequencing of HUVECs 48h after transfection with either gapmeRs targeting *MIRIAL* (20 nM) or control gapmeRs (control vs *MIRIAL* knockdown; colored dots fold change≥2; adj. $p \leq 0.01$.; $n=4$). **B** KEGG pathway analysis of RNA sequencing data in fig. 3A. **C** p53 target gene expression in HUVECs

48h after gapmeR-mediated *MIRIAL* knockdown (20 nM) compared to control-transfected HUVECs and siRNA-mediated knockdown of p53 (10 nM) or control transfected HUVECs, using qRT-PCR (n=5; Brown-Forsythe and Welch ANOVA). **D** Protein levels of p21 in HUVECs 48h after gapmeR-mediated *MIRIAL* knockdown (20 nM) compared to control-transfected HUVECs using Western Blot (n=4; unpaired t test). **E** Protein levels of p53 in HUVECs 48h after gapmeR-mediated *MIRIAL* knockdown (20 nM) compared to control-transfected HUVECs using Western Blot (n=4; unpaired t test). **F** Protein levels of phosphorylated p53 (Ser15) in HUVECs 48h after gapmeR-mediated *MIRIAL* knockdown (20 nM) compared to control-transfected HUVECs using Western Blot (n=4; unpaired t test). **G** *MIRIAL* expression measured by qRT-PCR after crosslinking and RNA immunoprecipitation (CLIP) of HUVEC lysate with a p53 antibody or IgG isotype control antibody (5 µg each) and Western blot analysis of p53 in the input and immunoprecipitates (n=3; unpaired t test). **H** Mitochondrial DNA (mtDNA) content relative to nuclear DNA (nDNA) content of HUVECs 48h after gapmeR-mediated *MIRIAL* knockdown (20 nM) compared to control-transfected HUVECs and siRNA-mediated knockdown of p53 (10 nM) or control transfected HUVECs using qPCR (n=3; ANOVA). Results are expressed as mean ± s.d.; *p<0.05, **p<0.01, ***p<0.001

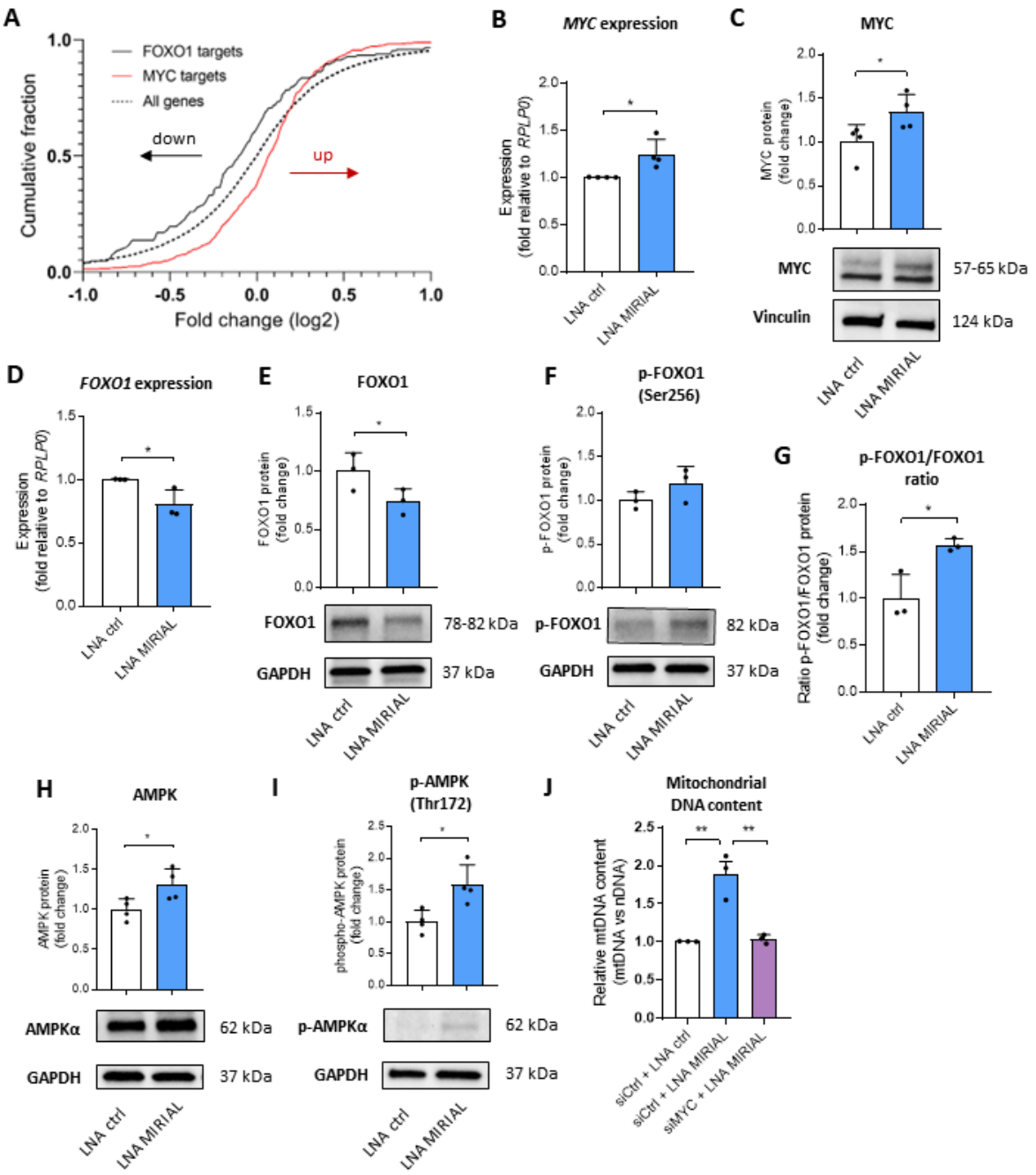

Fig. 4: *MIRIAL* regulates endothelial quiescence through FOXO1 and MYC

A Expression changes of MYC nuclear target genes encoding mitochondrial proteins and FOXO1 target genes compared to all genes 48h after gapmeR-mediated *MIRIAL* knockdown (20 nM) in HUVECs compared to control-transfected HUVECs using RNAseq (*n*=4). **B** *MYC* expression in HUVECs 48h after gapmeR-mediated *MIRIAL* knockdown (20 nM) compared to control-transfected HUVECs using qPCR (*n*=4; Mann-Whitney test). **C** Protein levels of MYC in

HUVECs 48h after gapmeR-mediated *MIRIAL* knockdown (20 nM) compared to control-transfected HUVECs using Western blot (n=4; Mann-Whitney test). **D** *FOXO1* expression in HUVECs 48h after gapmeR-mediated *MIRIAL* knockdown (20 nM) compared to control-transfected HUVECs using qRT-PCR (n=3; unpaired t test). **E** Protein levels of FOXO1 in HUVECs 48h after gapmeR-mediated *MIRIAL* knockdown (20 nM) compared to control-transfected HUVECs using Western blot (n=3; paired t test). **F** Protein levels of phosphorylated FOXO1 (Ser256) in HUVECs 48h after gapmeR-mediated *MIRIAL* knockdown (20 nM) compared to control-transfected HUVECs using Western blot (n=3; paired t test). **G** Ratio of phosphorylated to total protein levels of FOXO1 in HUVECs 48h after gapmeR-mediated *MIRIAL* knockdown (20 nM) compared to control-transfected HUVECs quantified from fig. 4 E and F (n=3; unpaired t test). **H** Protein levels of AMPK in HUVECs 48h after gapmeR-mediated *MIRIAL* knockdown (20 nM) compared to control-transfected HUVECs using Western blot (n=4; unpaired t test). **I** Protein levels of phosphorylated AMPK (Thr172) in HUVECs 48h after gapmeR-mediated *MIRIAL* knockdown (20 nM) compared to control-transfected HUVECs using Western blot (n=4; unpaired t test). **J** Mitochondrial DNA (mtDNA) content relative to nuclear DNA (nDNA) content of HUVECs 48h after gapmeR-mediated *MIRIAL* knockdown (20 nM) compared to control-transfected HUVECs and siRNA-mediated knockdown of MYC (60 nM) or control transfected HUVECs using qPCR (n=3; ANOVA). Results are expressed as mean ± s.d.; *p<0.05, **p<0.01

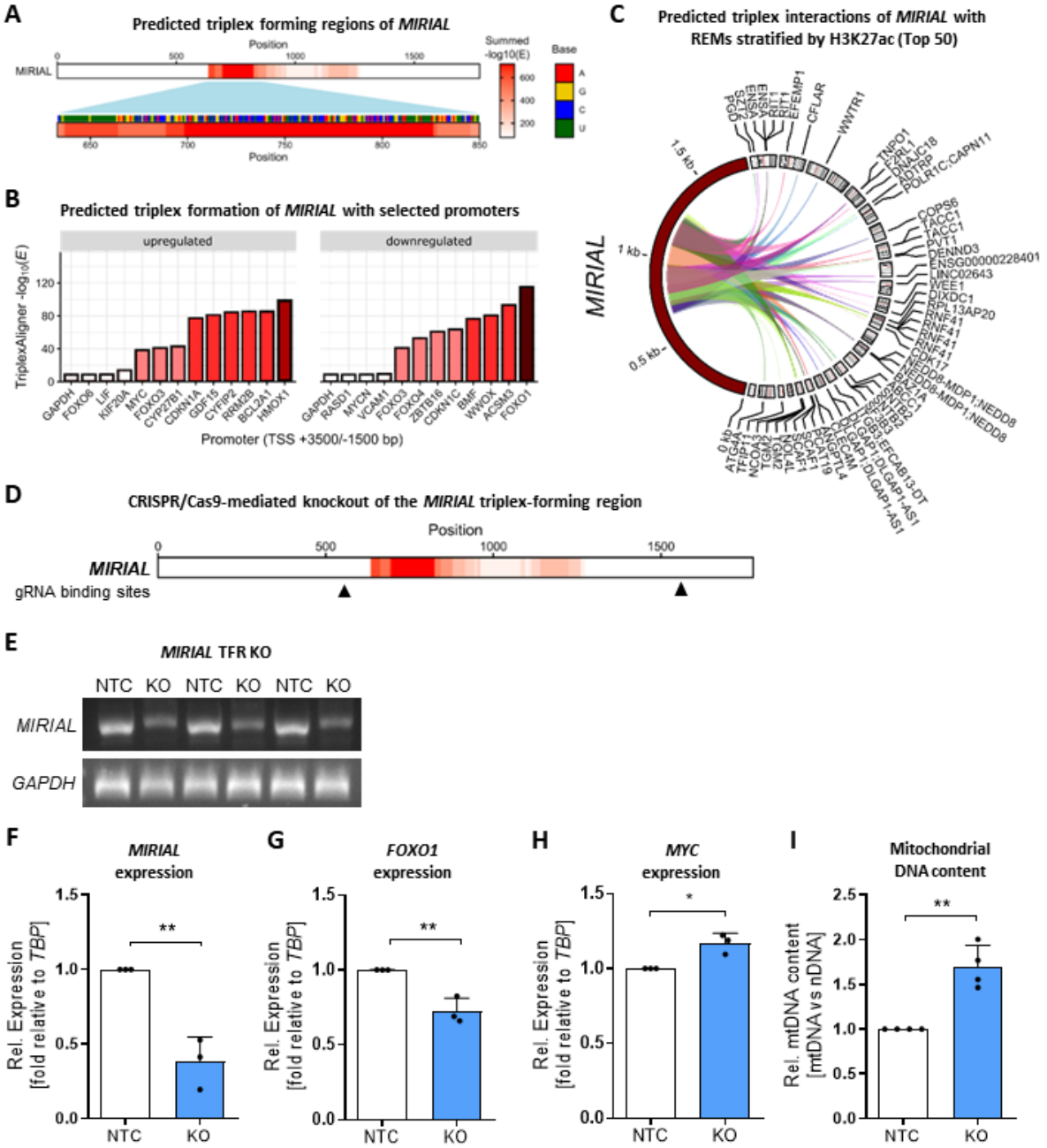

Fig. 5: *MIRIAL* forms *RNA*·DNA:DNA triplexes in the *FOXO1* promoter region

A Schematic representation of the lncRNA *MIRIAL* showing predicted probability (-log10(E) values) of *RNA*·DNA:DNA triplex forming regions (TFRs) in the lncRNA using *TriplexAligner*. **B** *TriplexAligner* scores (-log10(E) values) for predicted interactions between the lncRNA *MIRIAL* and selected promoters of genes upregulated after *MIRIAL* knockdown (*FOXO6, LIF, KIF20A, MYC, CYP27B1, CDKN1A, GDF15, CYFIP2, RRM2B, BCL2A1, HMOX1*) or downregulated after

MIRIAL knockdown (*RASD1, MYCN, VCAM1, FOXO4, ZBTB16, CDKN1C, BMF, WWOX, ACSM3, FOXO1*) in RNAseq (fig. 3A), in comparison to negative control promoters of genes that are not regulated after *MIRIAL* knockdown (*GAPDH* and *FOXO3*) using *TriplexAligner*. **C** Top 50 predicted triplex interactions of *MIRIAL* with regulatory elements (REMs) using *TriplexAligner* ranked by *TriplexAligner* score and stratified by genome accessibility (H3K27ac) data obtained from ENCODE. **D** Schematic representation of the *MIRIAL* transcript and the binding sites of guide RNAs (gRNAs) used for CRISPR/Cas9-mediated knockout (KO) of the triplex-forming region (TFR) of *MIRIAL*. **E** CRISPR/Cas9-mediated knockout (KO) of the *MIRIAL* TFR in HUVECs using lentiviral transduction of *MIRIAL*-targeting guide-RNAs or non-targeting control (NTC) gRNAs and measured my genomic DNA PCR 10 days post-transduction. *GAPDH* serves as loading control. Three independent experiments are shown. **F** *MIRIAL* expression after CRISPR/Cas9-mediated knockout (KO) of the *MIRIAL* TFR or non-targeting control (NTC) using qRT-PCR (n=3; unpaired t test). **G** *FOXO1* expression in HUVECs 10 days after CRISPR/Cas9-mediated *MIRIAL* TFR knockout compared to control-transduced HUVECs using qRT-PCR (n=3; unpaired t test). **H** *MYC* expression in HUVECs 10 days after CRISPR/Cas9-mediated *MIRIAL* TFR knockout compared to control-transduced HUVECs using qRT-PCR (n=3; unpaired t test). **I** Mitochondrial DNA (mtDNA) content relative to nuclear DNA (nDNA) content of HUVECs 10 days after CRISPR/Cas9-mediated *MIRIAL* TFR knockout compared to control-transduced HUVECs using qPCR (n=4; unpaired t test). Results are expressed as mean ± s.d.; *p<0.05, **p<0.01

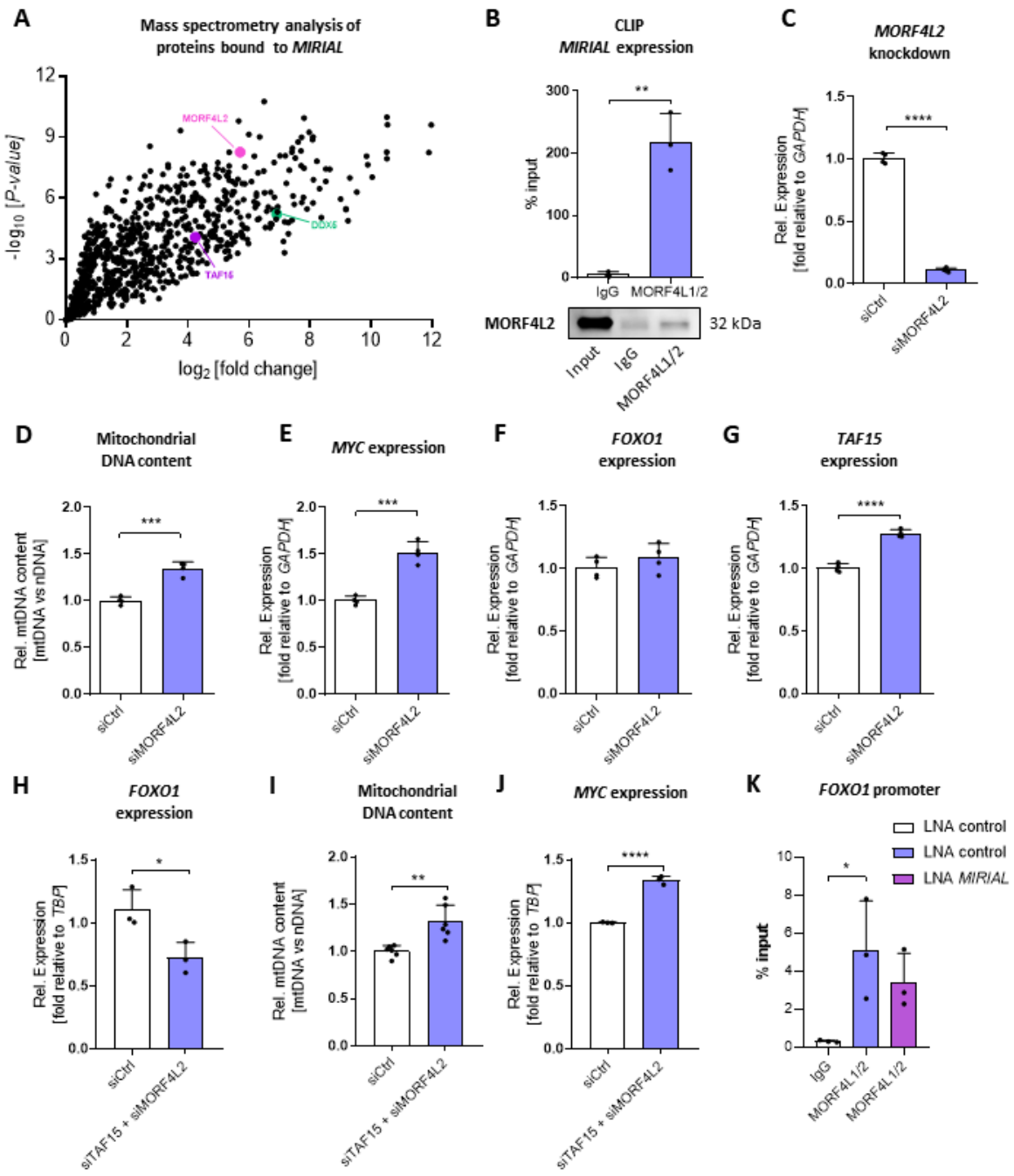

Fig. 6: *MIRIAL* recruits Mortality Factor 4 Like 2 (MORF4L2) and TATA-binding Protein-associated Factor 2N (TAF15) to the *FOXO1* transcriptional start site

A Volcano plot depicting all proteins from nuclear lysates enriched in *MIRIAL* pulldown as compared to pulldown with a scrambled oligo, identified by mass spectrometry (*n*=6; unpaired *t* test). **B** *MIRIAL* expression measured by qRT-PCR after crosslinking and RNA immunoprecipitation (CLIP) of HUVEC lysate with a MORF4L1/2 antibody or IgG isotype

control antibody (5 µg each) and Western blot analysis of MORF4L2 in the input and immunoprecipitates (*n*=3; unpaired *t* test). **C** *MORF4L2* expression in HUVECs 48h after siRNA-mediated *MORF4L2* knockdown (10 nM) compared to control-transfected HUVECs using qRT-PCR (*n*=4; unpaired *t* test). **D** Mitochondrial DNA (mtDNA) content relative to nuclear DNA (nDNA) content in HUVECs 48h after siRNA-mediated *MORF4L2* knockdown (10 nM) compared to control-transfected HUVECs using qPCR (*n*=4; unpaired *t* test). **E** *MYC* expression in HUVECs 48h after siRNA-mediated *MORF4L2* knockdown (10 nM) compared to control-transfected HUVECs using qRT-PCR (*n*=4; unpaired *t* test). **F** *FOXO1* expression in HUVECs 48h after siRNA-mediated *MORF4L2* knockdown (10 nM) compared to control-transfected HUVECs using qRT-PCR (*n*=4; unpaired *t* test). **G** *TAF15* expression in HUVECs 48h after siRNA-mediated *MORF4L2* knockdown (10 nM) compared to control-transfected HUVECs using qRT-PCR (*n*=4; unpaired *t* test). **H** *FOXO1* expression in HUVECs 48h after siRNA-mediated knockdown of *MORF4L2* and *TAF15* (10 nM each) compared to control-transfected HUVECs using qRT-PCR (*n*=3; unpaired *t* test). **I** Mitochondrial DNA (mtDNA) content relative to nuclear DNA (nDNA) content in HUVECs 48h after siRNA-mediated knockdown of *MORF4L2* and *TAF15* (10 nM each) compared to control-transfected HUVECs using qPCR (*n*=6; unpaired *t* test). **J** *MYC* expression in HUVECs 48h after siRNA-mediated knockdown of *MORF4L2* and *TAF15* (10 nM each) compared to control-transfected HUVECs using qRT-PCR (*n*=3; unpaired *t* test). **K** *FOXO1* promoter sequence measured by qPCR in HUVEC nuclear lysates after chromatin immunoprecipitation (ChIP) using a MORF4L1/2 antibody or IgG isotype control antibody (5 µg each). ChIP was performed 48 h after gapmeR-mediated knockdown of *MIRIAL* (20 nM) and compared to control-transfected HUVECs (*n*=3; ANOVA). Results are expressed as mean ± s.d.; **p*<0.05, ***p*<0.01, ****p*<0.001, *****p*<0.0001

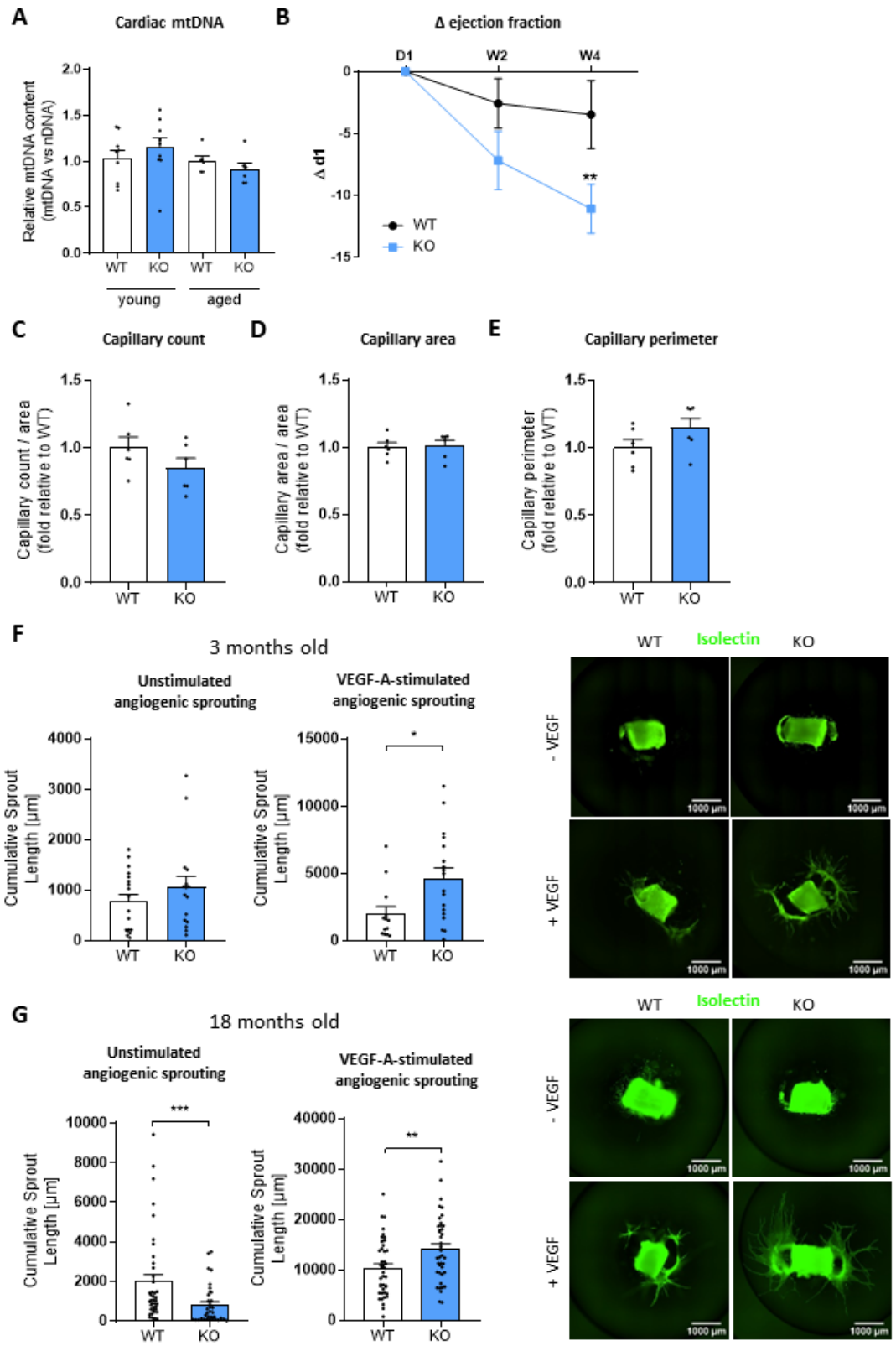

Fig. 7: *Mirial* KO in mice decreases EF after acute myocardial infarction and regulates angiogenic sprouting *ex vivo*

A Mitochondrial DNA (mtDNA) content relative to nuclear DNA (nDNA) content in heart tissue of young (3 months) and aged (18 months) *Mirial* KO mice and their WT littermates using qPCR (*n*=9 and 6 mice per group; ANOVA). **B** Cardiac contractile function of *Mirial* KO mice and their wildtype (WT) littermates assessed by echocardiography displayed as delta ejection fraction values two weeks (W2) or four weeks (W4) after AMI in comparison to day 1 (D1) (*n*=6; ANOVA). **C** Capillary count in serial cardiac sections of the infarct border zone 4 weeks after AMI surgery of *Mirial* KO mice (11-13 weeks) and their wildtype (WT) littermates. ECs were stained using Isolectin B4 and analyzed using confocal microscopy. Representative images are shown in supp. fig. 8E. Per mouse, three sections were analyzed (*n*=6; unpaired *t* test). **D** Capillary area in serial cardiac sections of the infarct border zone 4 weeks after AMI surgery of *Mirial* KO mice (11-13 weeks) and their wildtype (WT) littermates. ECs were stained using Isolectin B4 and analyzed using confocal microscopy. Representative images are shown in supp. fig. 8E. Per mouse, three sections were analyzed (*n*=6; Mann-Whitney test). **E** Capillary perimeter in serial cardiac sections of the infarct border zone 4 weeks after AMI surgery of *Mirial* KO mice (11-13 weeks) and their wildtype (WT) littermates. ECs were stained using Isolectin B4 and analyzed using confocal microscopy. Representative images are shown in supp. fig. 8E. Per mouse, three sections were analyzed (*n*=6; unpaired *t* test). **F** Cumulative sprout length from aortic rings of young (3 months) *Mirial* KO mice and WT littermates under basal and VEGF-stimulated (30 ng/mL) conditions (*n*=6 mice per group; Mann-Whitney test). ECs were stained with Isolectin B4 and analyzed using immunofluorescence microscopy. 2-8 aortic rings per mouse were analyzed. **G** Cumulative sprout length from aortic rings of aged (18 months) *Mirial* KO mice and WT littermates under basal and VEGF-stimulated (30 ng/mL) conditions (*n*=6 mice per group; Mann-Whitney test and unpaired *t* test). ECs were stained with Isolectin B4 and analyzed using immunofluorescence microscopy. 5-8 aortic rings per

mouse were analyzed. Results are expressed as mean ± s.e.m.; *$p<0.05$, **$p<0.01$, ***$p<0.001$

Supplemental Materials

1. Supplemental figures and legends

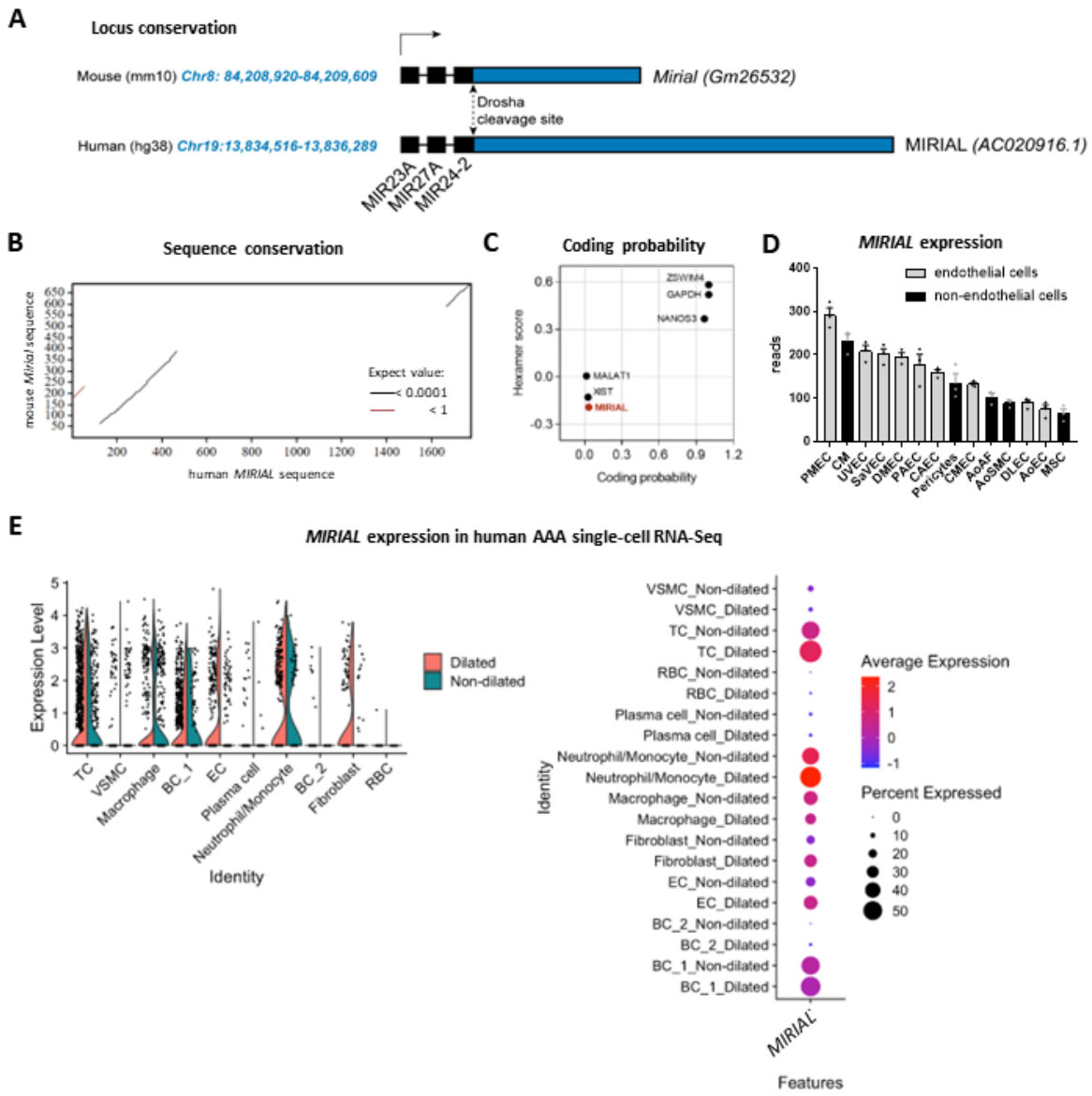

Supp. Fig. 1: A Schematic representation of the orthologous *Mirial* (Gm26532) and *MIRIAL* (AC020916.1) loci in mouse and human, respectively, including the chromosome coordinates and the miRNA cluster miR-23A~27A~24-2. **B** Sequence conservation between mouse *Mirial* (y-axis) and human *MIRIAL* (x-axis) using the LALIGN DNA:DNA tool of the FASTA Sequence Comparison software of the University of Virginia. **C** Coding probability of *MIRIAL* compared to established non-coding transcripts (*MALAT1* and *XIST*) and protein-coding transcripts

(*GAPDH* and *NANOS3*) as well as the nearest protein-coding gene to the *MIRIAL* locus (*ZSWIM4*) using the Coding-Potential Assessment Tool (CPAT). **D** *MIRIAL* expression in human endothelial cells (ECs) from different vascular beds (PMEC = Pulmonary Microvascular ECs, UVEC = Umibilical Vein ECs, SaVEC = Saphenous Vein ECs, DMEC = Dermal Microvascular ECs, PAEC = Pulmonary Arterial ECs, HCAEC = Coronary Artery ECs, CMEC = Cardiac Microvascular ECs, DLEC = Dermal Lymphatic ECs, AoEC = Aortic ECs) and non-endothelial cardiovascular cells (CM = cardiomyocytes, pericytes, AoAF = Aortic Arterial Fibroblasts, AoSMC = Aortic Smooth Muscle Cells, MSC = mesenchymal stem cells) measured by RNA sequencing (*n*=3). Results are expressed as mean ± s.e.m. **E** Violin plot and dot plot showing the expression pattern of *MIRIAL* in identified cell clusters in abdominal aortic aneurysm (AAA) patient samples (dilated) compared to undilated control samples from the same patients using single-cell RNA sequencing (TC = T Cells, VSMC = Vascular Smooth Muscle Cells, BC = B cells, EC = Endothelial Cells, RBC = Red Blood Cells) (*n*=4).

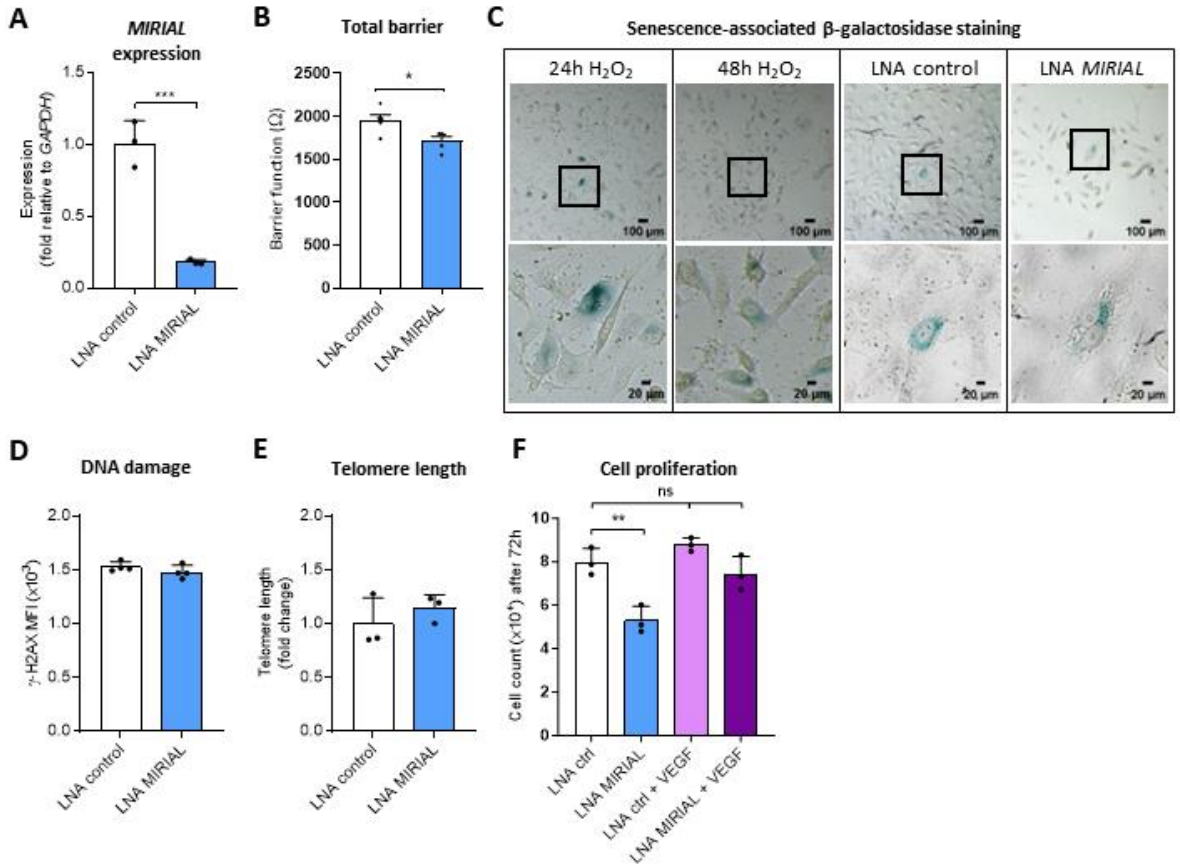

Supp. Fig. 2: A *MIRIAL* expression in HUVECs 48h after gapmeR-mediated *MIRIAL* knockdown (20 nM) compared to control-transfected HUVECs using qRT-PCR (*n*=3; unpaired *t* test). **B** Electric cell-substrate impedance sensing (ECIS)-based measurement of the endothelial barrier function of HUVECs 48h after gapmeR-mediated *MIRIAL* knockdown (20 nM) compared to control-transfected HUVECs (*n*=5; unpaired *t* test). **C** Representative images of senescence-associated β-galactosidase staining in HUVECs 48h after gapmeR-mediated *MIRIAL* knockdown (20 nM) compared to control-transfected HUVECs. Treatment of untransfected HUVECs with H_2O_2 (200 µM) for 24h or 48h, respectively, was included as a positive control. **D** DNA damage in HUVECs 48h after gapmeR-mediated *MIRIAL* knockdown (20 nM) compared to control-transfected HUVECs measured by γH2A.X (Ser139) staining followed by flow cytometry (*n*=4; unpaired *t* test). **E** Telomere length in HUVECs 48h after gapmeR-mediated *MIRIAL* knockdown (20 nM) compared to control-transfected HUVECs

measured by qPCR (*n*=3; unpaired *t* test). **F** Proliferation of HUVECs measured as cell count 72h post-transfection. HUVECs were transfected with a gapmeR targeting *MIRIAL* or a negative control gapmeR (20 nM) and treated with VEGF-A (50 ng/mL) or vehicle (PBS) (*n*=3; ANOVA). Results are expressed as mean ± s.d.; *$p<0.05$, **$p<0.01$

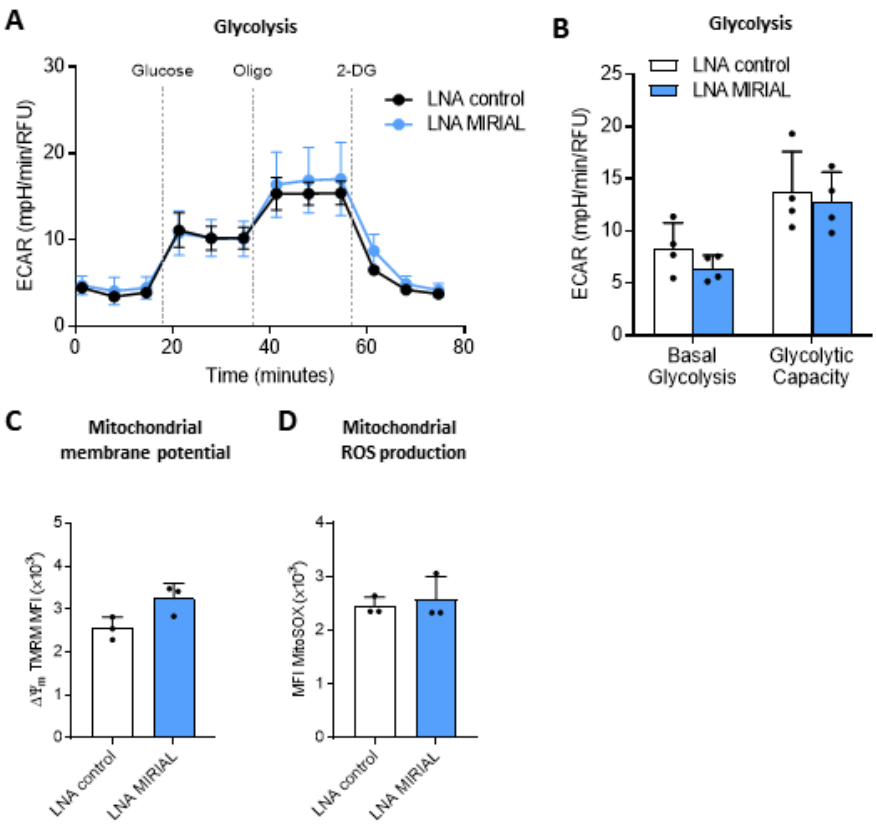

Supp. Fig. 3: A Extracellular acidification rate (ECAR) as a measure of glycolysis in HUVECs 48h after gapmeR-mediated *MIRIAL* knockdown (20 nM) compared to control-transfected HUVECs using the Seahorse glycolysis stress test (representative graph of *n*=4). **B** Extracellular acidification rate (ECAR) as a measure of basal glycolysis and glycolytic capacity in HUVECs 48h after gapmeR-mediated *MIRIAL* knockdown (20 nM) compared to control-transfected HUVECs using the Seahorse glycolysis stress test, quantification from supp. fig. 3A (*n*=4; ANOVA). **C** Mitochondrial membrane potential in HUVECs 48h after gapmeR-mediated *MIRIAL* knockdown (20 nM) compared to control-transfected HUVECs measured by tetramethylrhodamine-methylester (TMRM) staining followed by flow cytometry (*n*=3; unpaired *t* test). **D** Mitochondrial production of reactive oxygen species (ROS) in HUVECs 48h after gapmeR-mediated *MIRIAL* knockdown (20 nM) compared to control-transfected HUVECs measured by MitoSOX staining followed by flow cytometry (*n*=3; Mann-Whitney test). Results are expressed as mean ± s.d.

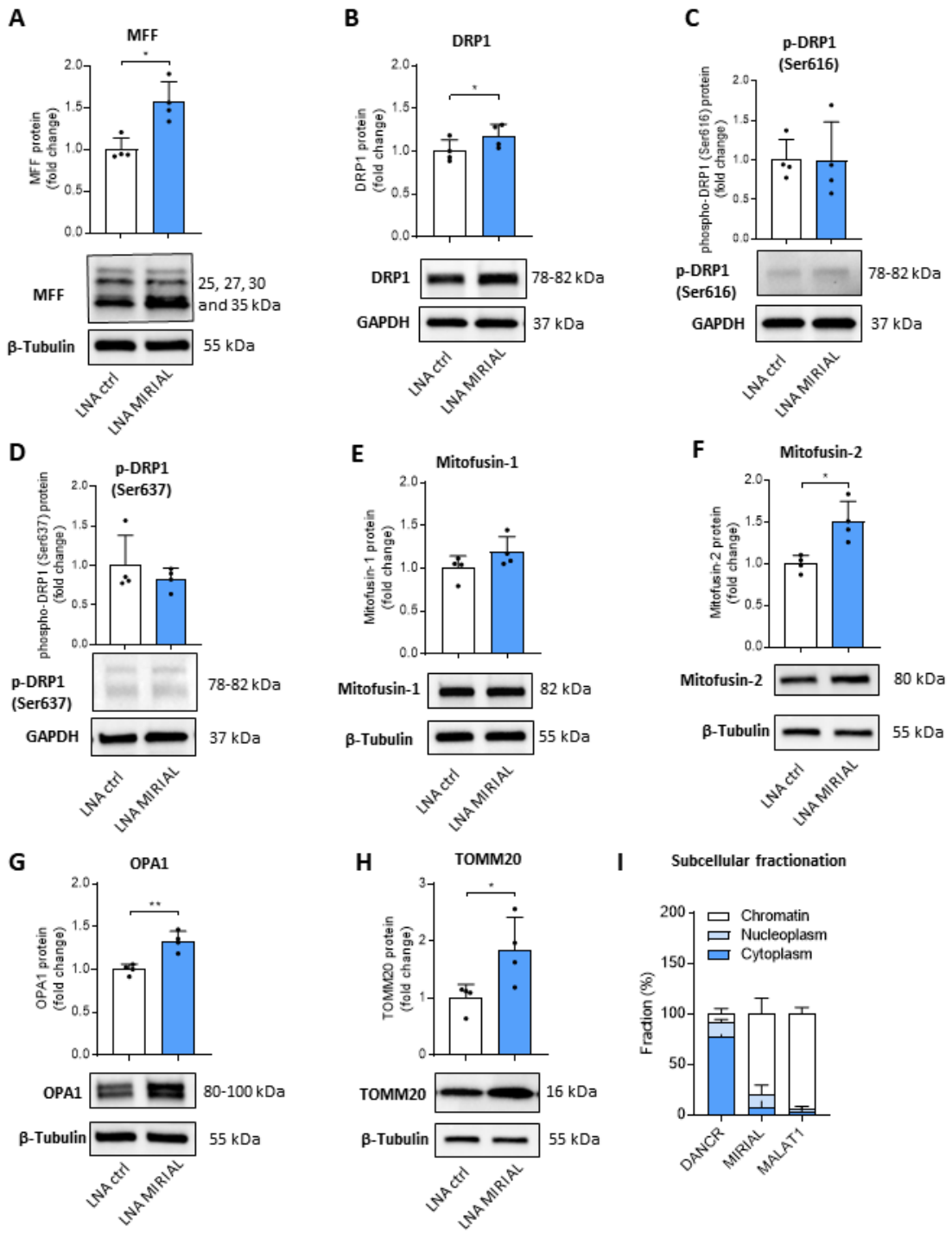

Supp. Fig. 4: A Protein levels of MFF in HUVECs 48h after gapmeR-mediated *MIRIAL* knockdown (20 nM) compared to control-transfected HUVECs using Western Blot (*n*=4; Mann-Whitney test). **B** Protein levels of DRP1 in HUVECs 48h after gapmeR-mediated *MIRIAL* knockdown (20 nM) compared to control-transfected HUVECs using Western Blot (*n*=4; paired *t* test). **C** Protein levels of phosphorylated DRP1 (Ser616) in HUVECs 48h after gapmeR-

mediated *MIRIAL* knockdown (20 nM) compared to control-transfected HUVECs using Western Blot (*n*=4; paired *t* test). **D** Protein levels of phosphorylated DRP1 (Ser637) in HUVECs 48h after gapmeR-mediated *MIRIAL* knockdown (20 nM) compared to control-transfected HUVECs using Western Blot (*n*=4; Mann-Whitney test). **E** Protein levels of Mitofusin-1 in HUVECs 48h after gapmeR-mediated *MIRIAL* knockdown (20 nM) compared to control-transfected HUVECs using Western Blot (*n*=4; paired *t* test). **F** Protein levels of Mitofusin-2 in HUVECs 48h after gapmeR-mediated *MIRIAL* knockdown (20 nM) compared to control-transfected HUVECs using Western Blot (*n*=4; paired *t* test). **G** Protein levels of OPA1 in HUVECs 48h after gapmeR-mediated *MIRIAL* knockdown (20 nM) compared to control-transfected HUVECs using Western Blot (*n*=4; paired *t* test). **H** Protein levels of TOMM20 in HUVECs 48h after gapmeR-mediated *MIRIAL* knockdown (20 nM) compared to control-transfected HUVECs using Western Blot (*n*=4; Mann-Whitney test). **I** Expression of the lncRNAs *DANCR*, *MIRIAL* and *MALAT1* in HUVEC subcellular fractions (cytoplasm, nucleoplasm and chromatin) using qRT-PCR (*n*=3). Results are expressed as mean ± s.d.; *$p<0.05$, **$p<0.01$

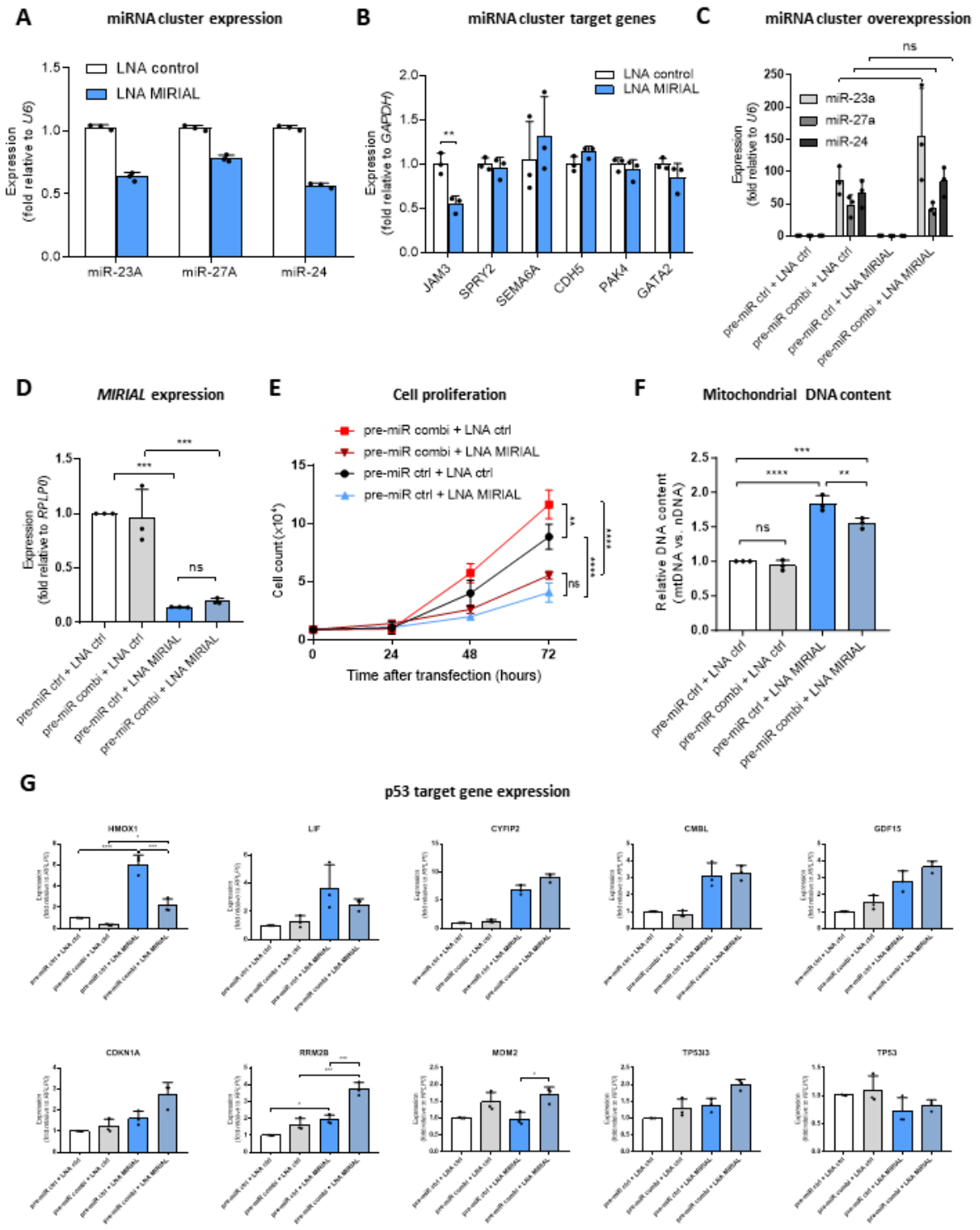

Supp. Fig. 5: A Expression of the miRNAs miR-23A, miR-27A and miR-24-2 in HUVECs 48h after gapmeR-mediated *MIRIAL* knockdown (20 nM) compared to control-transfected HUVECs measured using TaqMan qRT-PCR (*n*=3; Kruskal-Wallis test). **B** Expression of selected target genes of miR-23A (*JAM3* and *SPRY2*), miR-27A (*SEMA6A* and *CDH5*) and miR-24-2 (*PAK4* and

GATA2) in HUVECs 48h after gapmeR-mediated *MIRIAL* knockdown (20 nM) compared to control-transfected HUVECs measured using qRT-PCR (*n*=3; ANOVA). **C** Overexpression of the miRNAs miR-23A, miR-27A and miR-24-2 measured using TaqMan qRT-PCR. HUVECs were transfected for 48h with a mix of equal amounts (10 nM each) of precursor miRNAs of miR-23A, miR-27A and miR-24-2 (pre-miR combi) or a negative pre-miR-control (30 nM) and a gapmeR targeting *MIRIAL* or a negative control gapmeR (20 nM) (*n*=3; ANOVA). **D** *MIRIAL* expression using qRT-PCR. HUVECs were transfected for 48h with a mix of equal amounts (10 nM each) of precursor miRNAs of miR-23A, miR-27A and miR-24-2 (pre-miR combi) or a negative pre-miR-control (30 nM) and a gapmeR targeting *MIRIAL* or a negative control gapmeR (20 nM) (*n*=3; ANOVA). **E** Growth curve depicting the cell number of HUVECs after the indicated hours (0-72h) post-transfection. HUVECs were transfected with a mix of equal amounts (10 nM each) of precursor miRNAs of miR-23A, miR-27A and miR-24-2 (pre-miR combi) or a negative pre-miR-control (30 nM) and a gapmeR targeting *MIRIAL* or a negative control gapmeR (20 nM) (representative graph of *n*=3; ANOVA). **F** Mitochondrial DNA (mtDNA) content relative to nuclear DNA (nDNA) content in HUVECs 48h post-transfection using qPCR. HUVECs were transfected with a mix of equal amounts (10 nM each) of precursor miRNAs of miR-23A, miR-27A and miR-24-2 (pre-miR combi) or a negative pre-miR-control (30 nM) and a gapmeR targeting *MIRIAL* or a negative control gapmeR (20 nM) (*n*=3; ANOVA). **G** Expression of *TP53* and p53 target genes regulated after *MIRIAL* knockdown (fig. 3A and 3C) in HUVECs 48h post-transfection using qRT-PCR. HUVECs were transfected for 48h with a mix of equal amounts (10 nM each) of precursor miRNAs of miR-23A, miR-27A and miR-24-2 (pre-miR combi) or a negative pre-miR-control (30 nM) and a gapmeR targeting *MIRIAL* or a negative control gapmeR (20 nM) (*n*=3; ANOVA or Kruskal-Wallis test). Results are expressed as mean ± s.d.; *$p<0.05$, **$p<0.01$, ***$p<0.001$, ****$p<0.0001$

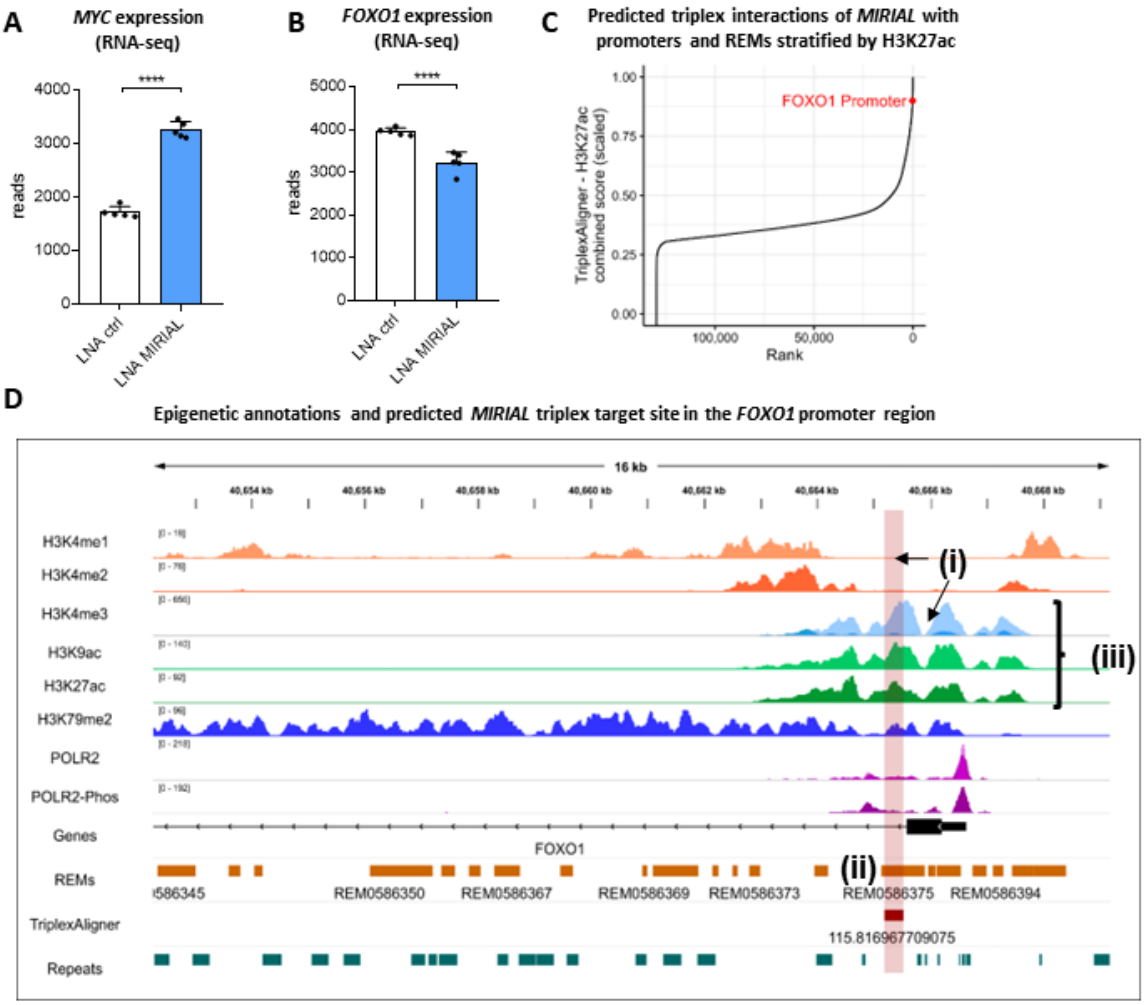

Supp. Fig. 6: A *MYC* expression in HUVECs 48h after gapmeR-mediated *MIRIAL* knockdown (20 nM) compared to control-transfected HUVECs measured by RNA sequencing (*n*=6; Mann-Whitney test with FDR correction). **B** *FOXO1* expression in HUVECs 48h after gapmeR-mediated *MIRIAL* knockdown (20 nM) compared to control-transfected HUVECs measured by RNA sequencing (*n*=6; Mann-Whitney test with FDR correction). **C** All predicted interactions of *MIRIAL* with regulatory elements (REMs) and promoters, stratified by H3K27ac signal. When *TriplexAligner* score and H3K27ac signal in the triplex site are combined, the *FOXO1* promoter region target site of *MIRIAL* is in ranked #188 (top 0.15%) of more than 150,000 potential *MIRIAL* target regions. Scaled score = $\log_{10}$(*TriplexAligner* –$\log_{10}$(E) × H3K27ac signal in target site) scaled to between 0 & 1. **D** Epigenetic annotations and predicted *MIRIAL* triplex target site in the *FOXO1* promoter region illustrated using the Integrative Genomics Viewer

(IGV). (i) The *MIRIAL* target site is distinct from the transcription factor binding sites at the *FOXO1* promoter. (ii) The predicted *MIRIAL* target site in the *FOXO1* promoter region covers multiple REMs. (iii) The target site is an active regulatory region with chromatin highly decorated with H3K27ac, H3K9ac and H3K4me3. Results are expressed as mean ± s.d.; ****$p<0.0001$

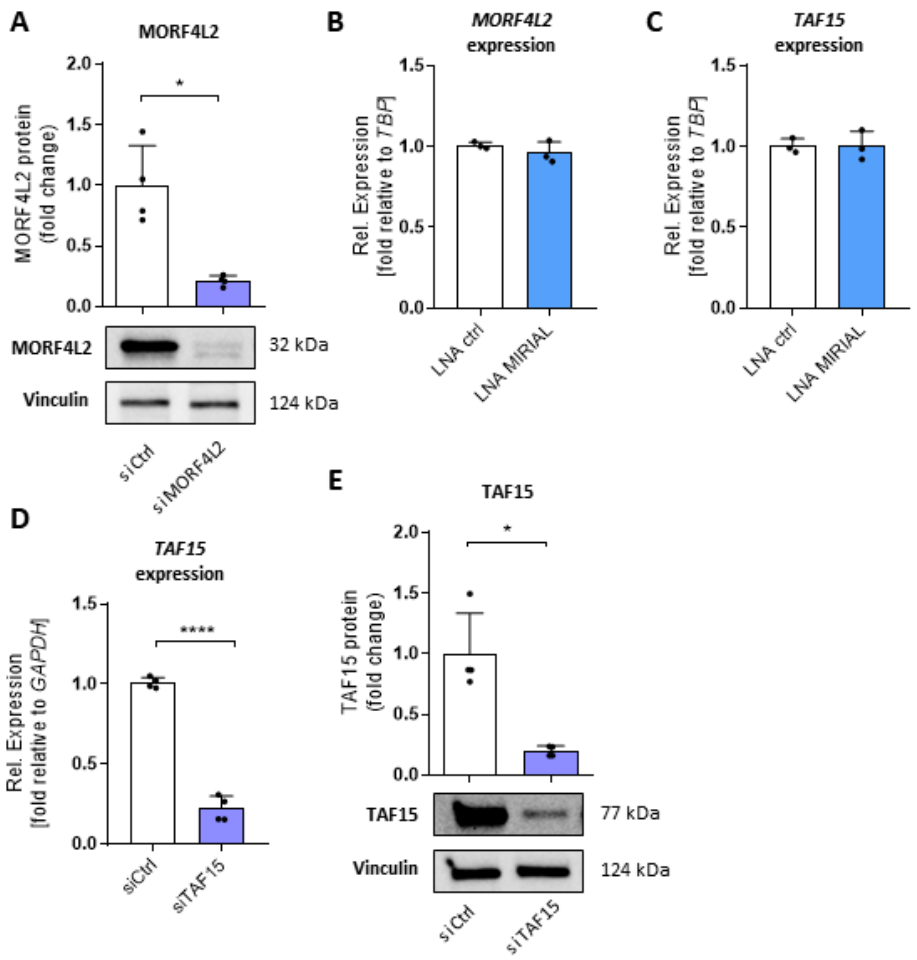

Supp. Fig. 7: A Protein levels of MORF4L2 in HUVECs 48h after siRNA-mediated *MORF4L2* knockdown (10 nM) compared to control-transfected HUVECs using Western Blot (*n*=4; paired *t* test). **B** *MORF4L2* expression in HUVECs 48h after gapmeR-mediated *MIRIAL* knockdown (20 nM) compared to control-transfected HUVECs using qRT-PCR (*n*=3; unpaired *t* test). **C** *TAF15* expression in HUVECs 48h after gapmeR-mediated *MIRIAL* knockdown (20 nM) compared to control-transfected HUVECs using qRT-PCR (*n*=3; unpaired *t* test). **D** *TAF15* expression in HUVECs 48h after siRNA-mediated *TAF15* knockdown (10 nM) compared to control-transfected HUVECs using qRT-PCR (*n*=4; unpaired *t* test). **E** Protein levels of TAF15 in HUVECs 48h after siRNA-mediated *TAF15* knockdown (10 nM) compared to control-transfected HUVECs using Western Blot (*n*=4; Mann-Whitney test). Results are expressed as mean ± s.d.; *$p<0.05$, ****$p<0.0001$

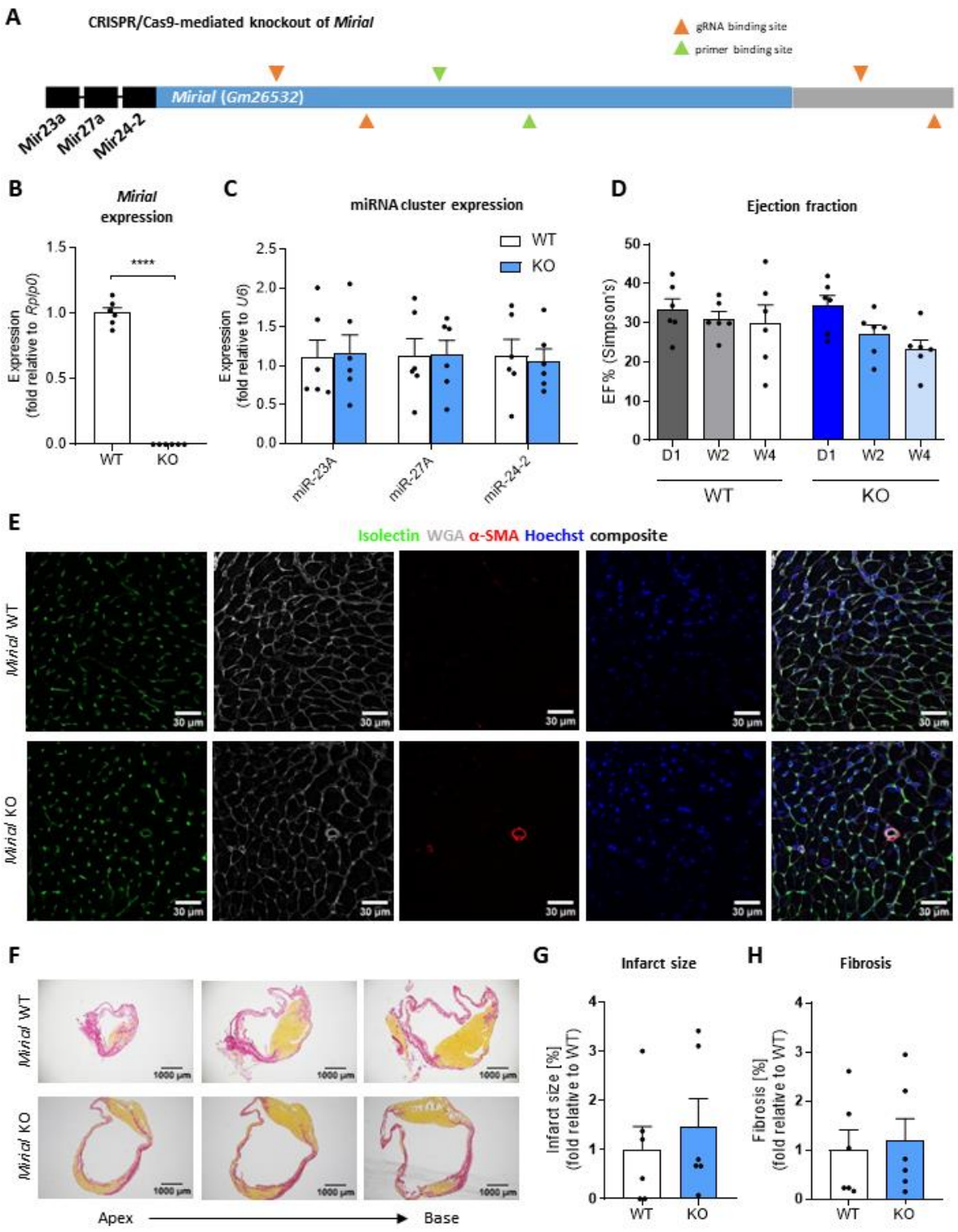

Supp. Fig. 8: A Schematic representation of the *Mirial* locus including the miR-23a~27a~24-2 cluster and the binding sites of guide RNAs (gRNAs) used for CRISPR/Cas9-mediated knockout (KO) of *Mirial* in mice as well as primer binding sites to detect the KO using qRT-PCR. **B** *Mirial* expression in the lungs of *Mirial* KO mice (13-14 weeks) and their wildtype (WT) littermates

using qRT-PCR (*n*=6; unpaired *t* test). **C** Expression of the miRNAs miR-23A, miR-27A and miR-24-2 in the lungs of *Mirial* KO mice (13-14 weeks) and their wildtype (WT) littermates using TaqMan qRT-PCR (*n*=6; ANOVA). **D** Cardiac contractile function of *Mirial* KO mice and their wildtype (WT) littermates assessed by echocardiography on day one (D1), two weeks (W2) or four weeks (W4) after AMI surgery displayed as percent ejection fraction values (*n*=6; unpaired *t* test). **E** Representative images of serial sections of the heart of *Mirial* KO mice and their WT littermates four weeks after AMI surgery stained with Isolectin (ECs), wheat germ agglutinin (WGA) (all cell membranes), anti-alpha smooth muscle actin (SMA) (vascular smooth muscle cells of larger vessels) and Hoechst33342 (nuclei). Images were obtained from the infarct border zone using confocal microscopy. **F** Representative images of serial sections of the heart of *Mirial* KO mice and their WT littermates four weeks after AMI surgery stained with Sirius Red. **G** Infarct size quantified from serial sections of the heart of *Mirial* KO mice and their WT littermates four weeks after AMI surgery stained with Sirius Red and shown in supp. fig. 8F. Infarct size was assessed by measuring the length of the infarcted region as percentage of the left ventricular circumference (*n*=6; unpaired *t* test). **H** Fibrosis quantified from serial sections of the heart of *Mirial* KO mice and their WT littermates four weeks after AMI surgery stained with Sirius Red and shown in supp. fig. 8F. Fibrosis was assessed by measuring the positively stained area as percentage of the total area of the section (*n*=6; unpaired *t* test). Results are expressed as mean ± s.e.m.; ****$p<0.0001$

2. Major Resources Table

Animals (in vivo studies)

Species	Vendor or Source	Background Strain	Sex	Persistent ID / URL
Mouse	Janvier	C57Bl/6	both	https://janvier-labs.com/en/fiche_produit/3_aged_c57bl-6jrj_mouse/ https://janvier-labs.com/en/fiche_produit/2_c57bl-6jrj_mouse/
Mouse	Cyagen/Taconic	*Mirial* KO	both	-

Antibodies

Target antigen	Vendor or Source	Catalogue #	Working concentration	Persistent ID / URL
Actin α, smooth muscle, Cy3	Sigma-Aldrich	C6198	1:300	https://www.sigmaaldrich.com/DE/de/product/sigma/c6198
AMPKa (D63G4)	Cell Signaling	5832	1:1000	https://www.cellsignal.com/products/primary-antibodies/ampka-d63g4-rabbit-mab/5832
c-Myc	Cell Signaling	9402	1:500	https://www.cellsignal.com/products/primary-antibodies/c-myc-antibody/9402
FOXO1 (C29H4)	Cell Signaling	2880	1:1000	https://www.cellsignal.com/products/primary-antibodies/foxo1-c29h4-rabbit-mab/2880
GAPDH (14C10)	Cell Signaling	2118	1:2000	https://www.cellsignal.com/products/primary-antibodies/gapdh-14c10-rabbit-mab/2118
Goat anti-mouse HRP	Agilent Dako	P0447	1:2000	https://www.agilent.com/en/product/specific-proteins/elisa-kits-accessories/goat-anti-mouse-immunoglobulins-hrp-affinity-isolated-2717109
Goat anti-rabbit Alexa Fluor 488	Thermo Fisher	A32731	1:100	https://www.thermofisher.com/antibody/product/Goat-anti-Rabbit-IgG-H-L-Highly-Cross-Adsorbed-Secondary-Antibody-Polyclonal/A32731
Goat anti-rabbit HRP	Agilent Dako	P0448	1:2000	https://www.agilent.com/en/product/specific-proteins/elisa-kits-accessories/goat-anti-rabbit-immunoglobulins-hrp-affinity-isolated-2717113
H2AX (pS139) PE	BD Bioscience	562377	1:100	https://www.bdbiosciences.com/en-de/products/reagents/flow-cytometry-reagents/research-reagents/single-color-antibodies-ruo/pe-mouse-anti-h2ax-ps139.562377
Mitochondrial Dynamics Antibody	Cell Signaling	74792	1:1000	https://www.cellsignal.com/products/primary-antibodies/mitochondrial-dynamics-antibody-sampler-kit-ii/74792

Sampler Kit II				
MORF4L1/2	Santa Cruz	sc-514659	5 µg	https://www.scbt.com/p/morf4-l1-2-antibody-d-9?requestFrom=search
MORF4L2	Novus Bio	NBP2-47370	1:1000	https://www.novusbio.com/products/morf4l2-antibody_nbp2-47370
Normal mouse IgG	Santa Cruz	sc-2025	5 µg	https://www.scbt.com/de/p/normal-mouse-igg
p21, WAF1, CIP1 (12D1)	Cell Signaling	2947	1:1000	https://www.cellsignal.com/products/primary-antibodies/p21-waf1-cip1-12d1-rabbit-mab/2947
p53	Cell Signaling	9282	1:500	https://www.cellsignal.com/products/primary-antibodies/p53-antibody/9282
p53 (1C12)	Cell Signaling	2524	5 µg	https://www.cellsignal.com/products/primary-antibodies/p53-1c12-mouse-mab/2524
Phospho-AMPKa (Thr172) (D4D6D)	Cell Signaling	50081	1:1000	https://www.cellsignal.com/products/primary-antibodies/phospho-ampka-thr172-d4d6d-rabbit-mab/50081
phospho-FOXO1 (Ser256) (E1F7T)	Cell Signaling	84192	1:1000	https://www.cellsignal.com/products/primary-antibodies/phospho-foxo1-ser256-e1f7t-rabbit-mab/84192
Phospho-p53 (Ser15)	Cell Signaling	9284	1:1000	https://www.cellsignal.com/products/primary-antibodies/phospho-p53-ser15-antibody/9284
TAF15	Cell Signaling	28409	1:1000	https://www.cellsignal.com/products/primary-antibodies/taf15-d8v6q-rabbit-mab/28409
TOM20	Santa Cruz	sc-11415	1:100	https://www.scbt.com/p/tom20-antibody-fl-145?requestFrom=search
Vinculin XP (E1E9V)	Cell Signaling	13901	1:2000	https://www.cellsignal.com/products/primary-antibodies/vinculin-e1e9v-xp-174-rabbit-mab/13901
β-Tubulin (9F3)	Cell Signaling	2128	1:2000	https://www.cellsignal.com/products/primary-antibodies/b-tubulin-9f3-rabbit-mab/2128

Cultured Cells

Name	Vendor or Source	Sex (F, M, or unknown)	Persistent ID / URL
HUVECs, pooled	Lonza	unknown	https://bioscience.lonza.com/lonza_bs/DE/en/Primary-and-Stem-Cells/p/000000000000184943/HUVEC-%E2%80%93-Human-Umbilical-Vein-Endothelial-Cells%2C-Pooled%2C-in-EGM%E2%84%A2
Lenti-X 293T	Takara	unknown	https://www.takarabio.com/products/gene-function/viral-transduction/lentivirus/packaging-systems-and-cells/lenti-x-293t-cells

Data & Code Availability

Description	Source / Repository	Persistent ID / URL
RNA sequencing data set Control vs *MIRIAL* knockdown	GEO accession number GSE248795	https://www.ncbi.nlm.nih.gov/geo/query/acc.cgi?acc=GSE248795
RNA sequencing data set AAA	GEO accession number GSE237230	https://www.ncbi.nlm.nih.gov/geo/query/acc.cgi?acc=GSE237230 https://doi.org/10.1016/j.omtn.2023.08.017
RNA sequencing data set mouse cardiac endothelial cells	-	https://doi.org/10.1126/science.ade4961

Antisense oligonucleotides

ASO	Concentration	Sequence
LNA *MIRIAL*	20 nM	GGCATTTAACGGTCTG
siRNA Control	10-60 nM	CGUACGCGGAAUACUUCGA
siRNA MORF4L2	10 nM	AGGGTTGAATGAGTTCCAGAA
siRNA *MYC*	60 nM	GATCCCGGAGTTGGAAAACAA
siRNA *p53*	10 nM	CAGCATCTTATCCGAGTGGAA
siRNA *TAF15*	10 nM	TACGGTGGAGACCGAAGTGGA

miRNA precursors for miRNA overexpression (pre-miRs by ambion)

miRNA precursor	Concentration	Mature sequence
Hsa-miR-23a-3p	10 nM	AUCACAUUGCCAGGGAUUUCC
Hsa-miR-27a-3p	10 nM	UUCACAGUGGCUAAGUUCCGC
Hsa-miR-24-3p	10 nM	UGGCUCAGUUCAGCAGGAACAG

Human primers for q(RT)-PCR

Target	Strand	Sequence
36B4D	Fwd	CCCATTCTATCATCAACGGGTAC
36B4D	Rev	CAGCAAGTGGGAAGGTGTAATCC
CDKN1A	Fwd	GCGACTGTGATGCGCTAATG
CDKN1A	Rev	GAAGGTAGAGCTTGGGCAGG
CMBL	Fwd	CAGACTTCTTTGTAGGGCAAGAG
CMBL	Rev	GGCATGACACTGTTGTTTCAGA
CYFIP2	Fwd	TTCCGTATCCACCGTCCAAT
CYFIP2	Rev	CGCTGGGTAATGAGTCTGTTC
FOXO1	Fwd	GTCAAGACAACGACACATAG
FOXO1	Rev	AAACTAAAAGGGAGTTGGTG
FOXO1 promoter	Fwd	GAGATTTGGGGGAACGAAGC
FOXO1 promoter	Rev	CGAGGAGCCTCGATGTGGAT

GADPH	Fwd	GAGTCAACGGATTTGGTCGT
GADPH	Rev	TTGATTTTGGAGGGATCTCG
GDF15	Fwd	TAACCAGGCTGCGGGCCAAC
GDF15	Rev	CAGCCGCACTTCTGGCGTGA
HMOX1	Fwd	AGTCTTCGCCCCTGTCTACT
HMOX1	Rev	CTTCACATAGCGCTGCATGG
LIF	Fwd	TACGCCACCCATGTCACAAC
LIF	Rev	CTTGTCCAGGTTGTTGGGGA
MDM2	Fwd	CGAGCTTGGCTGCTTCTGG
MDM2	Rev	GTACGCACTAATCCGGGGAG
MIRIAL	Fwd	CCTAGCAGCCAGTTACCCAA
MIRIAL	Rev	TCCCGGCAAGTTAGAAAGCT
MIRIAL TFR KO	Fwd	ACTCCTGGCTTCCGGTATCA
MIRIAL TFR KO	Rev	AGGCAGGGAGGATCAGCTATT
MORF4L2	Fwd	AGAAGGAAGATTGTTGGTTG
MORF4L2	Rev	GCTGGTTCAAGATTTTTCTG
MT-ND1	Fwd	CCCTAAAACCCGCCACATCT
MT-ND1	Rev	GAGCGATGGTGAGAGCTAAGGT
MYC	Fwd	AGCTGCTTAGACGCTGGATTTT
MYC	Rev	TCGAGGTCATAGTTCCTGTTGG
PRKAA1	Fwd	TGTGATGGGATCTTCTATACC
PRKAA1	Rev	CCCTGATATCTTTGATTGTGG
RPLP0	Fwd	TCGACAATGGCAGCATCTAC
RPLP0	Rev	ATCCGTCTCCACAGACAAGG
RRM2B	Fwd	AGTTCTCGCCGGTTTGTCAT
RRM2B	Rev	AAGGAAGCCTGTGCCTGTTT
TAF15	Fwd	CAAAGCTATTCTGGCTATGG
TAF15	Rev	CTGGTTATTATATGGTTGCTGG
TBP	Fwd	GAGCTGTGATGTGAAGTTTCC
TBP	Rev	TCTGGGTTTGATCATTCTGTAG
Telomere	Fwd	GGTTTTTGAGGGTGAGGGTGAGGGTGAGGGTGAGGGT
Telomere	Rev	TCCCGACTATCCCTATCCCTATCCCTATCCCTATCCCTA
TP53	Fwd	TTTCACCCTTCAGATCCGTGG
TP53	Rev	AGTCTGAGTCAGGCCCTTCT
TP53I3	Fwd	TGGCTCTTGATGGTCGATGG
TP53I3	Rev	AGGCAGAATTTGCTCCGTGA

Mouse primers for q(RT)-PCR

Target	Strand	Sequence
Rplp0	Fwd	GCGTCCTGGCATTGTCTGT
Rplp0	Rev	GAAGGCCTTGACCTTTTCAGTAAG
Mirial KO	Fwd	GCTTTAGGCCCTCTAACGGT
Mirial KO	Rev	CTCGCTGTCACCAGCAGAAA
Mt-Nd1	Fwd	CTAGCAGAAACAAACCGGGC
Mt-Nd1	Rev	CCGGCTGCGTATTCTACGTTA

Other reagents

Description	Source / Repository	Persistent ID / URL
VEGF-A	PeproTech	https://www.peprotech.com/de/recombinant-human-vegfsub165sub
Isolectin B4	Vector	https://vectorlabs.com/products/biotinylated-gsl-i-isolectin-b4
Streptavidin-Alexa488	Invitrogen	https://www.thermofisher.com/order/catalog/product/S11223?SID=srch-srp-S11223
Endothelial Cell Basal Medium	Lonza	
EGM SingleQuots supplements	Lonza	
EZ-Magna ChIP G kit	Merck Millipore	https://www.sigmaaldrich.com/DE/de/product/mm/17409
Lipofectamine RNAiMax	Invitrogen	https://www.thermofisher.com/order/catalog/product/13778150
MultiScribe Reverse Transcriptase	Invitrogen	https://www.thermofisher.com/order/catalog/product/de/de/4311235
Fast SYBR Green Master Mix	Applied Biosystems	https://www.thermofisher.com/order/catalog/product/de/de/4385612

ARRIVE GUIDELINES

The ARRIVE guidelines (https://arriveguidelines.org/) are a checklist of recommendations to improve the reporting of research involving animals. Key elements of the study design should be included below to better enable readers to scrutinize the research adequately, evaluate its methodological rigor, and reproduce the methods or findings.

Study Design

Groups	Sex	Age	Number (prior to experiment)	Number (after termination)	Littermates (Yes/No)	Other description
wild type	both	11-13 weeks	8	6	yes	acute myocardial infarction model
Mirial KO	both	11-13 weeks	7	6	yes	acute myocardial infarction model
wild type	both	3 months, 18 months	12	12	yes	aortic ring assay
Mirial KO	both	3 months, 18 months	12	12	yes	aortic ring assay
wild type	both	13-14 weeks	6	6	yes	organ harvest
Mirial KO	both	13-14 weeks	6	6	yes	organ harvest

Sample Size: Please explain how the sample size was decided. Please provide details of any a *prior* sample size calculation, if done.

Because information on the function of *Mirial* in mice was lacking prior to this study, it was not feasible to conduct a power calculation. An estimate for the maximum sample size for a reliable phenotype was derived from published studies that utilized more than 12 animals per group. Considering the anticipated AMI mortality rate of approximately 25%, a maximum sample size of 16 animals per group was determined. However, given the minimal to absent phenotypic changes observed after AMI with a sample size of 6 animals per group, the authors opted not to utilize the maximum sample size.

Inclusion Criteria

Mice were included into experiments based on their age. For young mice, animals up to 14 weeks were chosen. For aged mice, animals between 17-20 months were included.

Exclusion Criteria

-

Randomization

-

Blinding

Researchers who performed AMI surgery, echocardiography, histology, and microscopic analyses of aortic rings were blinded.